

Products and dynamics of lava-snow explosions: The 16 March 2017 explosion at Mount Etna, Italy

R. Cioni^{1,†}, D. Andronico², L. Cappelli^{1,3}, A. Aravena^{4,5}, P. Gabellini¹, A. Cristaldi², R.A. Corsaro², M. Cantarero², F. Ciancitto², E. De Beni², and G. Ganci²

¹Dipartimento di Scienze della Terra, Università di Firenze, 50126, Firenze, Italy

²Istituto Nazionale di Geofisica e Vulcanologia, Osservatorio Etneo, Sezione di Catania, 95125, Catania, Italy

³Department of Geosciences, Environment and Society, Université Libre de Bruxelles, CP160/02 1050, Bruxelles, Belgium

⁴Facultad de Ciencias Básicas, Universidad Católica del Maule, 3480112, Talca, Chile

⁵Millennium Institute on Volcanic Risk Research—Ckelar Volcanoes, 1270709, Antofagasta, Chile

ABSTRACT

Volcanic hazards associated with lava flows advancing on snow cover are often underrated, although sudden explosions related to different processes of lava-snow/ice contact can occur rapidly and are only preceded by small, easily underrated precursors. On 16 March 2017, during a mildly effusive and explosive eruption at Mount Etna, Italy, a slowly advancing lava lobe interacted with the snow cover to produce a sudden, brief sequence of explosions. White vapor, brown ash, and coarse material were suddenly ejected, and the products struck a group of people, injuring some of them. The proximal deposit formed a continuous mantle of ash, lapilli, and decimeter-sized bombs, while the ballistic material travelled up to 200 m from the lava edge. The deposit was estimated to have a mass of $7.1 \pm 0.8 \times 10^4$ kg, which corresponds to a volume of 32.0 ± 3.6 m³ of lava being removed by the explosion. Data related to the texture and morphology of the ejected clasts were used to constrain a model of lava-snow interaction. The results suggest that the mechanism causing the explosions was the progressive build-up of pressure due to vapor accumulation under the lava flow, while no evidence was found for the occurrence of fuel-coolant interaction processes. Although these low-intensity explosions are not particularly frequent, the data set collected provides, for the first time, quantitative information about the processes involved and the associated hazard and suggests that


mitigation measures should be established to prevent potentially dramatic accidents at worldwide volcanoes frequented by tourists and with fairly easy access, such as Etna.

1. INTRODUCTION

The interaction of magma with water, ice, or snow can trigger phreatic and phreatomagmatic explosions that are potentially dangerous due to their impulsive and unpredictable nature (Lorenz, 1987; Wilson et al., 2013). Explosive hydromagmatic activity occurs when magma coming in direct contact with surface or subsurface water induces a sudden vaporization of water, greatly increasing magmatic explosivity. However, phreatic activity is generally related to the vaporization of mainly non-magmatic fluids that accumulate in subsurface aquifers (Barberi et al., 1992; Browne and Lawless, 2001; Caudron et al., 2018). Explosions driven by heated and vaporized surface fluids are frequent in volcanic environments and are generally related to the direct interaction of lava or pyroclastic flows with liquid water (sea or lakes/rivers) or ice/snow. Subglacial lava intrusions are very common and have been widely described in glacierized environments, such as Iceland, British Columbia, South America, and Antarctica (Wörner and Viereck, 1987; Stevenson et al., 2009; Smellie and Edwards, 2016). Supraglacial magma-ice/snow interaction is also quite common, and even apparently harmless volcanic phenomena, such as weakly fed lava flows, have episodically been observed to produce sudden explosions when traveling over a snow cover. The dynamics of these events have been studied by some authors (e.g., Vinogradov et al., 1990; Belousov et al., 2011; Edwards et al., 2012, 2013, 2015) at different volcanoes (e.g., Mount Etna, Italy; Fimmvörðuháls, Iceland; and Tolbachik,

Kamchatka, Russia). The scale of such explosions is variable, ranging from the formation of extended fields of rootless vents (e.g., Greeley and Fagents, 2001; Noguchi et al., 2016; Fagents and Thordarson, 2007) up to isolated explosions during the emplacement of slow-moving lava flows. Single gas-driven explosions originating close to the front or along the margins of a lava flow have also been sporadically reported in relation to methane production when vegetation buried by the advancing lava ignited (Kauahikaua, 2007). Interesting experimental work on lava-snow/ice interaction and the resulting dynamics of water melting and vapor formation was presented by Edwards et al. (2013), and the physics and thermodynamics of the process were investigated in relation to both subglacial (Höskuldsson and Sparks, 1997; Höskuldsson et al., 2006) and supraglacial eruptions (Wilson and Head, 2002, 2007; Wilson et al., 2013).

Mount Etna, Italy, one of the most active volcanoes in the world (Fig. 1A), represents a potential source of different volcanic hazards. In the past 20 years, its summit craters mainly produced lava fountaining and strong Strombolian activity (e.g., Andronico et al., 2014a, 2014b, 2021; Corsaro et al., 2017). The southeast crater (SEC) has been the most active, followed by the new southeast crater (NSEC) after 2011. The frequent activity of the NSEC caused a gradual coalescence with the SEC (Andronico et al., 2018), so that the two cones formed a unique apparatus that has been referred to as the SEC since November 2020 (INGV-OE, 2020). On 27 February 2017, an eruption started and initially produced lava effusion and Strombolian activity from a vent on the saddle separating the SEC from the NSEC, where it formed a small new cone. This short eruptive episode continued until 1 March 2017 (Andronico et al., 2017). On 15 March, vigorous

R. Cioni  <https://orcid.org/0000-0002-2526-9095>

[†]raffaello.cioni@unifi.it

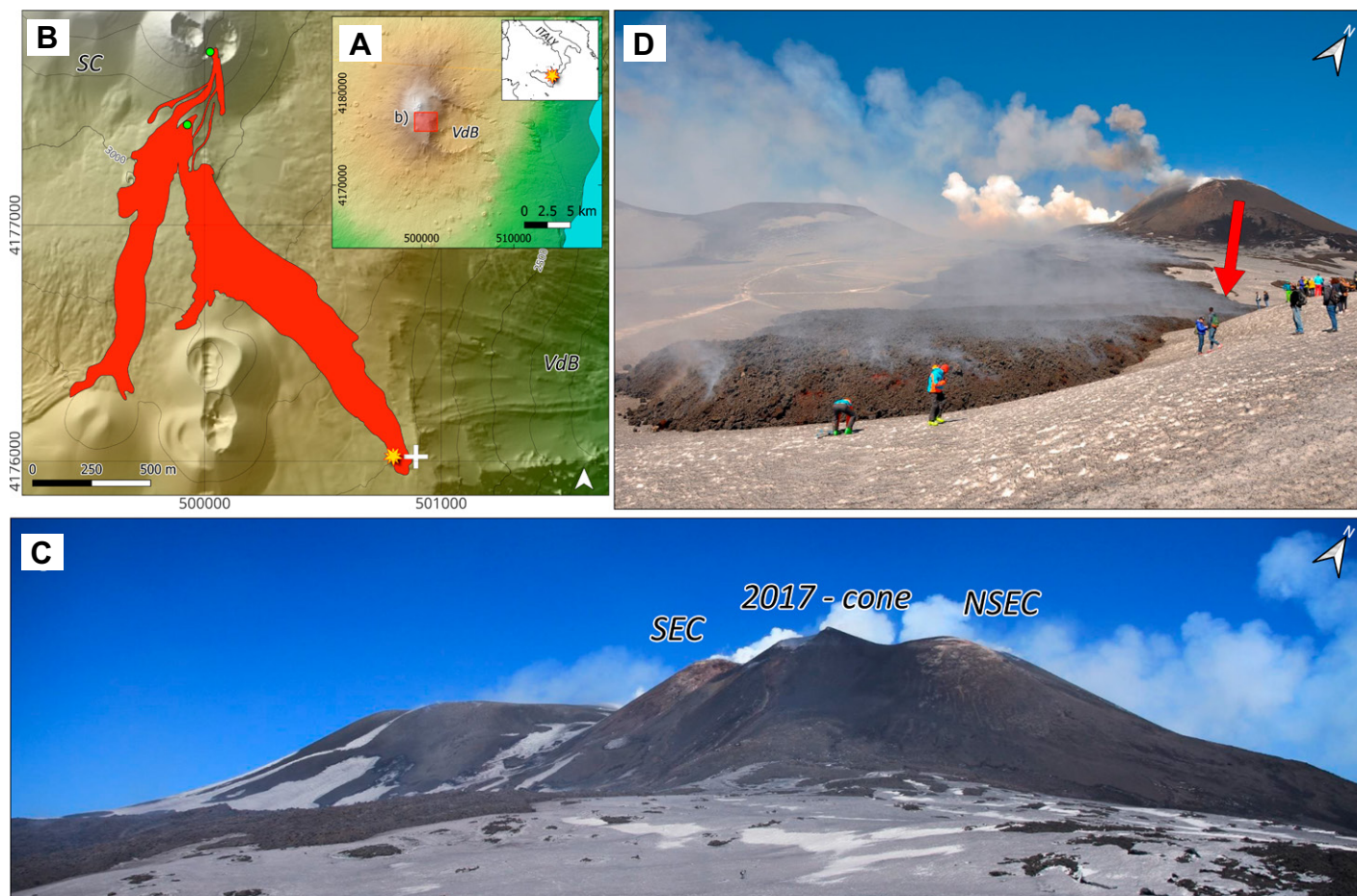


Figure 1. (A) Shaded relief map of Mount Etna volcano using the TINITALY DEM (Tarquini et al., 2012). Red rectangle delimits the study area. (B) Extension of the lava flow on 16 March 2017 (red area). Redrawn from satellite imagery (European Space Agency's Copernicus Open Access Hub, Sentinel-2A MSI, collected 16 March 2017, accessed 23 March 2023). Green dots indicate the two eruptive fissures that opened in February 2017. The white cross indicates the approximate location of the people near the lava flow front; yellow star indicates the epicenter of the explosion. SC—summit craters; VdB—Valle del Bove. High-resolution LiDAR elevation data are from Bisson et al. (2016). (C) Southeast crater–new southeast crater (SEC–NSEC) apparatus, showing the new cone that formed in 2017 between the two cones (image taken on 2 March 2017 by D. Andronico). (D) Eruptive activity on 16 March 2017, showing paroxysmal activity from the top of the SEC–NSEC apparatus and the eruptive fissure from which a lava flow was emitted on 16 March 2017. Red arrow indicates where increased degassing started several minutes before the explosive sequence. Note the people along the eastern lava flow boundary (image taken by F. Ciancitto).

Strombolian activity resumed at the new cone, while effusive activity began at an eruptive fissure, breaking the southern flank of the NSEC cone (Fig. 1B). The morning after, a volcanic plume from the new cone dispersed fine-grained particles to the SW. At the same time, a lava flow with a mean velocity of a few tens of meters per hour was descending from the fissure to the SE, where a group of at least 40 people had gathered even just a few meters from the lava's edge.

Heralded by increasing steam emission and ash puffs, the interaction of this slowly advancing lava lobe with the snow cover produced a fast and unexpected brief sequence of explosions. A British Broadcasting Company (BBC) crew, present on-site to record the eruptive activity of Etna, captured footage of the dramatic episode

(see R. Morelle, 16 March 2017, in Item S1 of the Supplemental Material¹), which was broadcast in near-real time worldwide.

¹Supplemental Material. Item S1: List of websites hosting the three videos discussed in the text. Item S2: UAS video footage of the lava flow and the deposit of the explosion. Figure S1: Effects of the explosions. Figure S2: Relative abundance of the different clast lithologies in the different samples. Figure S3: Shape parameters relative to grain-size class. Figure S4: Density distribution for the different lithologies of the coarse material. Figure S5: Pre-eruption topography of the area invaded by the lava flow. Table S1: Sample list. Data S1: Field and laboratory data. Please visit <https://doi.org/10.1130/GSAB.S.24088311> to access the supplemental material, and contact editing@geosociety.org with any questions.

In the first few days after the explosive sequence, surveys and an overflight by an unoccupied aerial system (UAS) were carried out by personnel of the Istituto Nazionale di Geofisica e Vulcanologia, Osservatorio Etno (INGV-OE), to collect representative samples and data on the dispersal area, thickness, and grain-size of the deposit produced by the explosive sequence. In the following weeks, further campaigns collected data on the mass load and lithology of the entire deposit and measured the size and weight of the largest clasts that had fallen in the proximal area (i.e., close to the source of the explosions). The main results derived from these field campaigns and the laboratory analyses of the volcanic products collected are presented here. This study represents,

to our knowledge, a unique case in which the products of a fully witnessed lava-snow explosion were studied in detail to quantify the main physical parameters that controlled its dynamics. Comprehensive study of the 16 March 2017 explosive sequence and products is crucial for evaluating the eruptive processes that control lava-snow explosions and could lead to risk mitigation in an area frequented by hundreds to thousands of tourists per day throughout the year.

2. NARRATIVE OF 16 MARCH 2017 EVENT

The 2017 explosive sequence was investigated through detailed analysis of images, news accounts, and videos available online. Three videos were used in the analysis: one, recorded by a camerawoman of the BBC, covers the first major explosion, while the other two cover the entire eruption sequence. The three videos (listed in the Supplemental Material) show some precursory events that possibly heralded the sequence of explosions (Fig. 1C). Photos taken by one of the authors (F. Ciancitto), who witnessed the event, were also carefully analyzed.

Overall, about 30 tourists accompanied by volcanological guides and INGV personnel with two snowmobiles were close to the front and edges of the lava flow during the explosions. Before the onset of the explosive sequence, most of the people were along the eastern flank or at the front of the active lava flow, at ~ 2700 m above sea level (a.s.l.; Fig. 1C).

2.1. Precursory Events

The explosive activity occurred when the front of the lava flow was nearly 2000 m from the vent, flanking a small, elongated hill to the east and advancing at a rate of $\sim 30\text{--}50$ m h^{-1} , according to field observations. A puff of steam preceded the main explosion by ~ 100 s (Fig. 2A). In the reconstructed chronology presented here, we consider the onset of the steaming as $t = 0$ (at 11:41:00 UTC) in all three videos. Weak and discontinuous puffs continued for ~ 8 s, until a loud sound was heard, and the steam emission gradually became more continuous and intense. Almost silently, a small emission of brownish ash occurred at $t = 39$ s, producing minor fallout around the emission point (Fig. 2B). At $t = 43$ s, the steam flux continued increasing in intensity and began to cross the lava flow transversely from east to west. One of the videos, recorded from around 2900 m a.s.l., ~ 500 m from and ~ 200 m upslope of the lava flow, clearly shows this increase in intensity (Fig. 2C). At $t = 63$ s,

preceded and accompanied by some loud sounds, two small ash plumes rose up from a more central area of the lava flow field (Fig. 2D), followed by a third small emission at $t = 83$ s. After the first small explosion, all of the videos show the volcanological guides urging the tourists to leave the area, clearly aware that it was no longer safe to stay close to or approach the lava flow.

2.2. The Sequence of Explosions

At $t = 89$ s, a sound much stronger than those heard during the previous ash emissions captured the attention of everyone nearby. This was followed by a first explosion that possibly formed a multiple jet. The BBC movie shows the launch of products ejected mostly to the west (Fig. 2E). Accordingly, the INGV-OE surveillance camera network shows that this explosion occurred at $\sim 11:42:30$ UTC ($t = 90$ s). A second explosion occurred after 3–4 s, some meters apart from the first one, producing an apparently smaller, subvertical single jet (Fig. 2F). We cannot exclude the rush/burst of other fast jets spatially and temporally close to these two main explosions, since meanwhile a dark brownish and dense ash cloud obscured the air, temporarily limiting visibility above and around the lava flow field. By that time, the videographers, now escaping from the area impacted, focused on people running to protect themselves from the fallout of volcanic material (Fig. 2G).

2.3. Effects of the Fallout of Volcanic Material

Immediately after the sequence of explosions, tourists were assisted by the guides and quickly transported downslope by a snowmobile; the roof and windows of one of the two vehicles for transporting tourists were damaged as well, even though it was parked a few tens of meters away from the lava flow. The fallout of incandescent material caused burns on most of the people's mountain clothing (Figs. S1A–S1E). According to news accounts, no one present was seriously injured (e.g., CataniaToday, 2017; La Repubblica, 2017). However, 10 people suffered wounds and urgently needed first aid care for head injuries and various burns, cuts, and bruises. Two of them were transported by helicopter directly from the Rifugio Sapienza (1920 m a.s.l.) to the hospital in Catania, where they remained for a few days. Two volcanological guides were hit by ballistics and suffered head trauma. Five tourists were hospitalized for minor skin abrasions and trauma at different hospitals in Catania and Acireale.

At least 30 min after the explosive sequence (i.e., as soon as the steam-ash mixture had completely dissipated and visibility was restored), F. Ciancitto went back to visit the area impacted by the fallout and found his glasses, which were lost during the escape, welded with a pyroclast, a tripod, and mountain equipment that were still burning (Figs. S1F–S1G). Notably, the high-temperature of part of the ejected material was confirmed during a preliminary thermal survey carried out at $\sim 17:00$ UTC, which documented the presence on the snow of large, scattered (pluri-decimeters in size) blocks that were still hot a few hours after being ejected (L. Lodato, personal commun., 2017).

It was immediately evident that the deposit was chaotic and mostly formed by lapilli-sized clasts (2–64 mm) and abundant ash, but also many blocks (or bombs) of several decimeters in dimension. A thin (< 10 cm), brownish, discontinuous muddy ash deposit was observed forming two main lobes that extended > 50 m from the lava flow front and was soon partially buried by the advancing lava.

3. METHODOLOGY

3.1. Field Surveys and Sampling

Several surveys were conducted to map the deposit above the snowpack and characterize the erupted products. Although the area impacted was relatively limited (Fig. 3A), we completed most of the fieldwork rapidly before the deposit could be covered by new explosive or effusive products of the ongoing eruption or disrupted by the seasonal melting of the snowpack. Given the small thickness of the fine-grained deposit and the scattered dispersal of coarse clasts, another non-trivial problem was to ensure representative sampling and characterization of the deposit in terms of areal variations, thickness, mass per unit area, grain-size, and clast lithology.

The first survey was carried out on 17 March 2017 to define the dispersal of the deposit (Fig. 3B), evaluate the original mass loading at different sites, and collect samples of the total deposit. We collected samples from seven sites with different percentages of area coverage and grain-size characteristics (i.e., areas of continuous, scattered, or highly scattered clast coverage; Fig. 4A and Table S1). At the same time, a UAS survey was carried out by the Cartographic Laboratory (MAP-LAB) of the INGV-OE (FlyEye Team), with a DJI Phantom 3 Professional flown at ~ 170 m above the take-off point located at ~ 2750 m a.s.l. in the middle of the deposit. Twenty-six images were used in Agisoft Metashape (<https://www.agisoft.com/>) structure from motion software covering 6.4×10^4 m^2 to

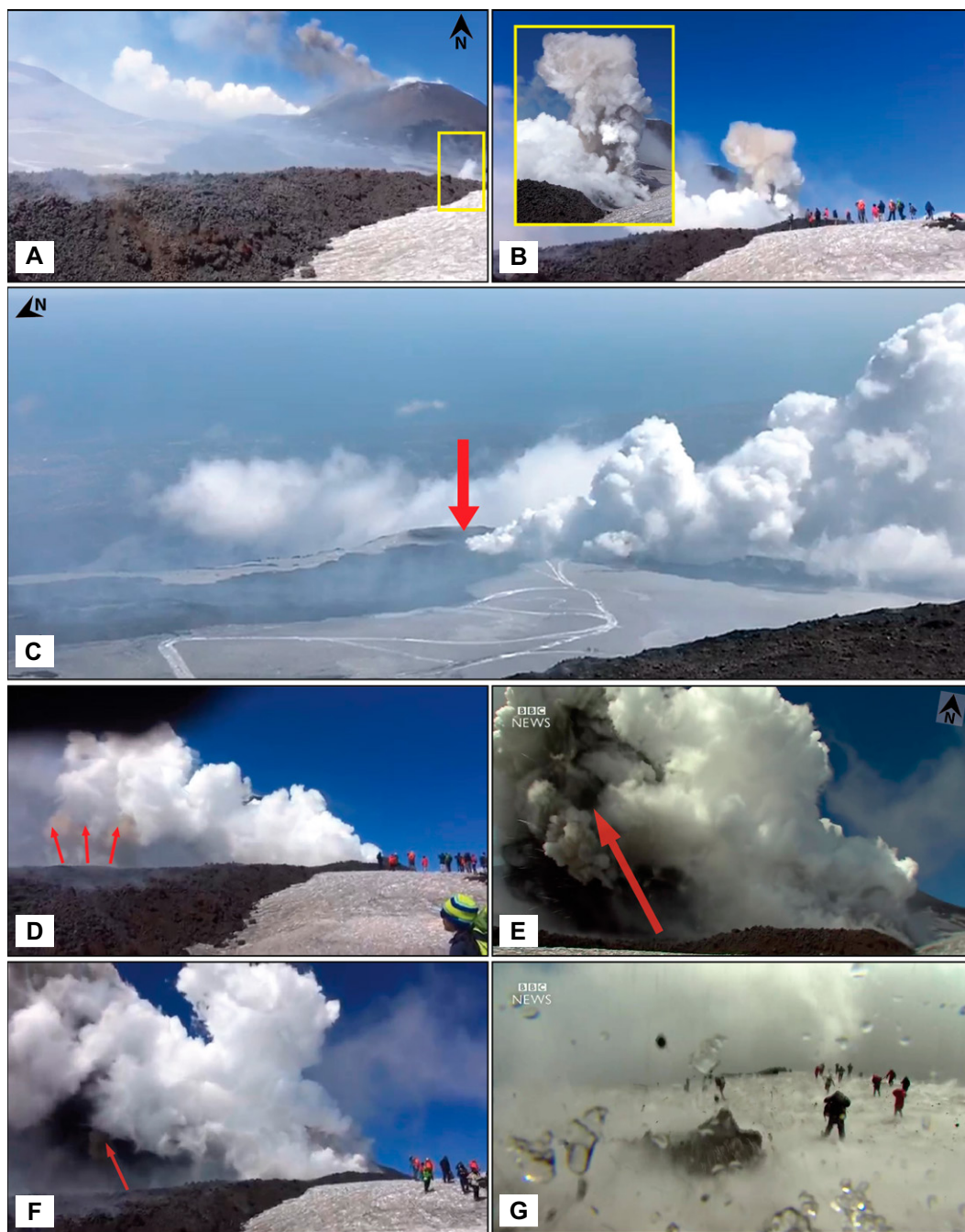


Figure 2. Images, extracted from videos recorded before and during the 16 March 2017 explosive sequence, showing the chronology of events (Morelle, 2017; courtesy of Magri Ernesto). (A) First puff of steam at $t = 0$ s. (B) First small ash puff at $t = 39$ s. Trajectories of several clasts are also easily viewed in the inset. (C) Increasing steam flux visible in frame A, recorded from around 2900 m a.s.l., i.e., upslope from the lava flow portion involved in the explosive sequence. (D) Two small ash plumes rising at $t = 63$ s, before the main burst. (E) First fan explosion, with coarse clasts launched to the left at $t = 89$ s. (F) Second large explosion visible in footage 3–4 s after the first explosion. (G) Frame showing tourists hurrying to escape. Frame C was extracted from a video kindly provided by an anonymous tourist.

produce an orthomosaic with a ground resolution of 6.21 cm/pixel (Fig. 3B). Another UAS survey conducted under the same flight conditions resulted in video footage of the entire lava field, which is presented in the Supplemental Material.

A week later, on 24 March 2017, a second survey was conducted to analyze the total mass of the scattered coarse material (clasts >10 cm) based on a set of sampling areas (Fig. 3B). Measurements were made along three different directions starting from the lava levee, with one

roughly corresponding to the main dispersal axis (i.e., $N246^\circ$) up to 140 m from the lava boundary, and the other two aligned along $N306^\circ$ and $N200^\circ$ (i.e., N and S of the main axis) and up to distances of 160 m and 190 m, respectively (Fig. 3B). Along the three trends, we studied a total of 21 sites, and for each site we delimited a square surface of 1 m² or 25 m² (depending on the coverage of clasts >10 cm) in which we measured the total mass of coarse material using an electronic hanging scale (maximum weight load: 40 kg; precision: 10 g). The weights were

then reduced by 5% to correct for the average humidity naturally retained by the samples, as estimated after oven-drying selected samples. At each area, we also weighed the three largest clasts and measured the three orthogonal axes (Bonadonna et al., 2013) using a metric ruler (precision 0.5 cm). During this survey, seven samples were collected for later analysis (samples PH13–PH19; Table S1).

Several months later (on 17 October 2017), we collected four single bombs coarser than 25 cm in diameter (PH20–PH23; Table S1). Addi-

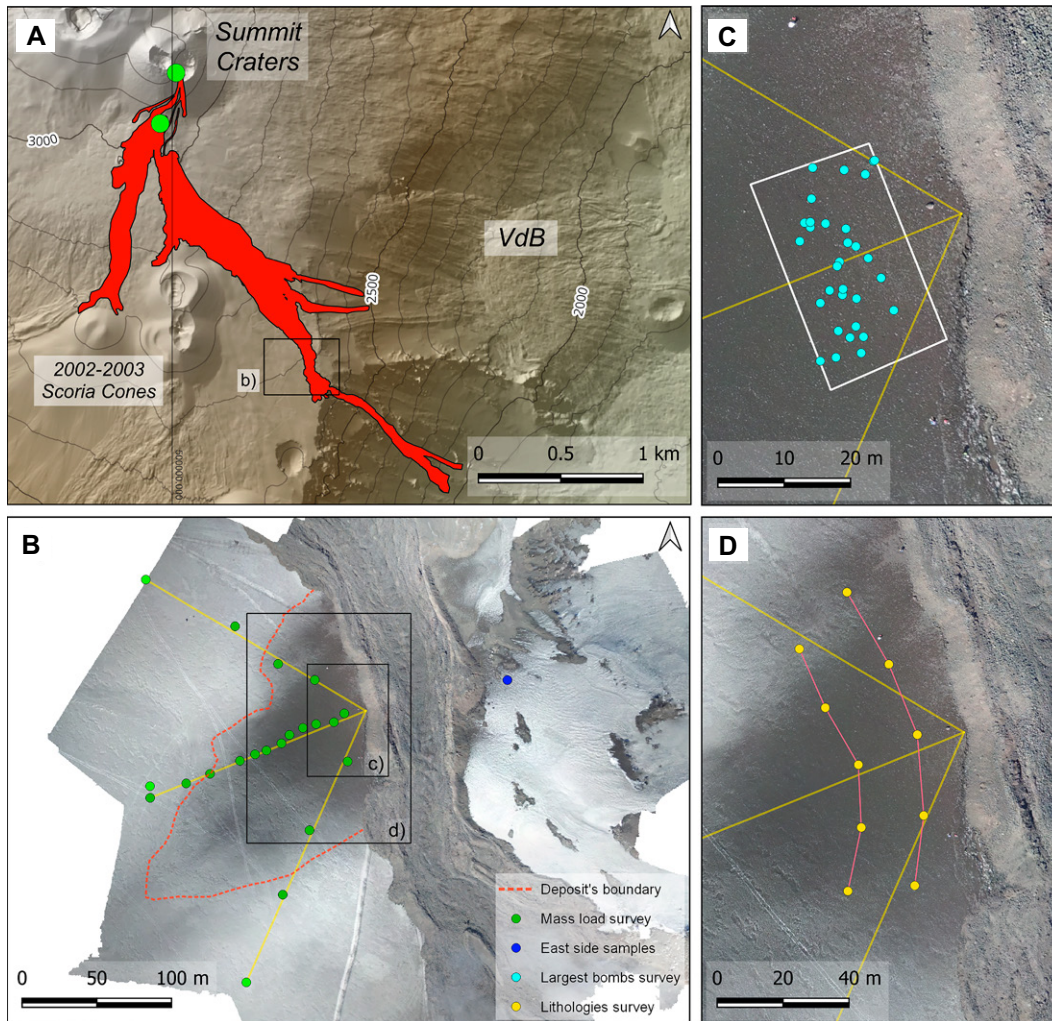


Figure 3. (A) Shaded relief map with contour lines every 100 m; red indicates the area of the lava flow that produced the event (modified from De Beni et al., 2021). VdB—Valle del Bove. High-resolution LiDAR elevation data are from Bisson et al. (2016). (B) Orthomosaic indicating the distribution of areas measured along three profiles; green circles indicate the center of each sampling area. In each area, the mass load of the deposit and the largest clasts were measured and weighed. (C) Location of the 30 largest clasts (blue dots, main axis >25 cm) measured and weighed in the proximal area. (D) Centers of the 4-m²-wide sampling areas of lapilli-sized clasts (yellow dots) collected for morphological characterization.

tionally, to estimate possible differences in the distribution of the largest bombs, we defined two adjacent square areas of 100 m² located at ~10 m from the lava levee on each side of the dispersal axis (Fig. 3C), and we measured the GPS positions of all clasts coarser than 25 cm. Differences in the lithology and distribution of the bombs were estimated at 10 square areas of 4 m² each, spaced ~25 m along two subparallel lines transversal to the dispersal axis (Fig. 3D). We recorded the GPS position at the center of each measured area, and in each we collected and classified a representative set of clasts (from 30 to 42), for a total of 355 clasts in the range of 32 mm and 64 mm ($\varphi = -5$, samples PH24–PH33; see Section 3.2 and Table S1).

After the eruption, the morphology of the lava near the explosion site was examined to reveal the presence of structures suggesting rootless vent(s) both from field observations and the analysis of aerial images taken during the drone survey by the INGV-OE FlyEye Team the day after the explosive sequence. The area on the

opposite boundary of the lava flow with respect to the main dispersal zone was also investigated, and only a few scattered decimeter-sized clasts delimiting an “upwind” outer rim of the deposit were found (samples PH11 and PH12; Fig. 3B and Table S1). Notably, the images from the 17 March 2017 flight did not show any evidence of explosion craters on the flow field. After the 16 March 2017 event, the feeding of the lava flow was, in fact, still very active, and finally obliterated the explosive source area.

In all, we collected 33 samples, PH1–PH33 (Table S1), from 30 different sites. Of the 33 collected samples, 10 samples (PH1–PH7, PH9, PH10, and PH18) are representative of the total deposits in each measured area (in two cases, fine- and coarse-grained portions were separated). The other samples (10 composed of 30–42 clasts in the range of 32 mm and 64 mm, PH24–PH33; six formed by selected bomb types, PH13–PH17 and PH19; four single bombs coarser than 25 cm in diameter, PH20–PH23; two clasts from the upwind side of the main tephra dispersal, PH11

and PH12; and one made up of different types of altered clasts, PH8) were collected to study the componentry and the main morphological and lithological characteristics of the coarse material, as well as to define any possible heterogeneity in the dispersal of coarse clasts.

3.2. Analytical Methods

Samples were analyzed at the Sedimentology and Optic Microscopy Laboratory (LSMO-OE) of INGV-OE, the Volcanology Laboratory of the Dipartimento di Scienze della Terra, Università di Firenze, Florence, Italy, and the Electron Microscopy and Microanalysis Service Center (MEMA-UNIFI) of the Università di Firenze. Grain-size analysis of the samples collected (Table S1) was carried out at LSMO-OE. The coarse-grained samples were mechanically sieved for the size range $-6 < \varphi < 0$ ($\varphi = -\log_2(d)$, where d is the particle diameter in mm), while the fine-grained portions ($\varphi > 0$) were analyzed with CAMSIZER, a digital

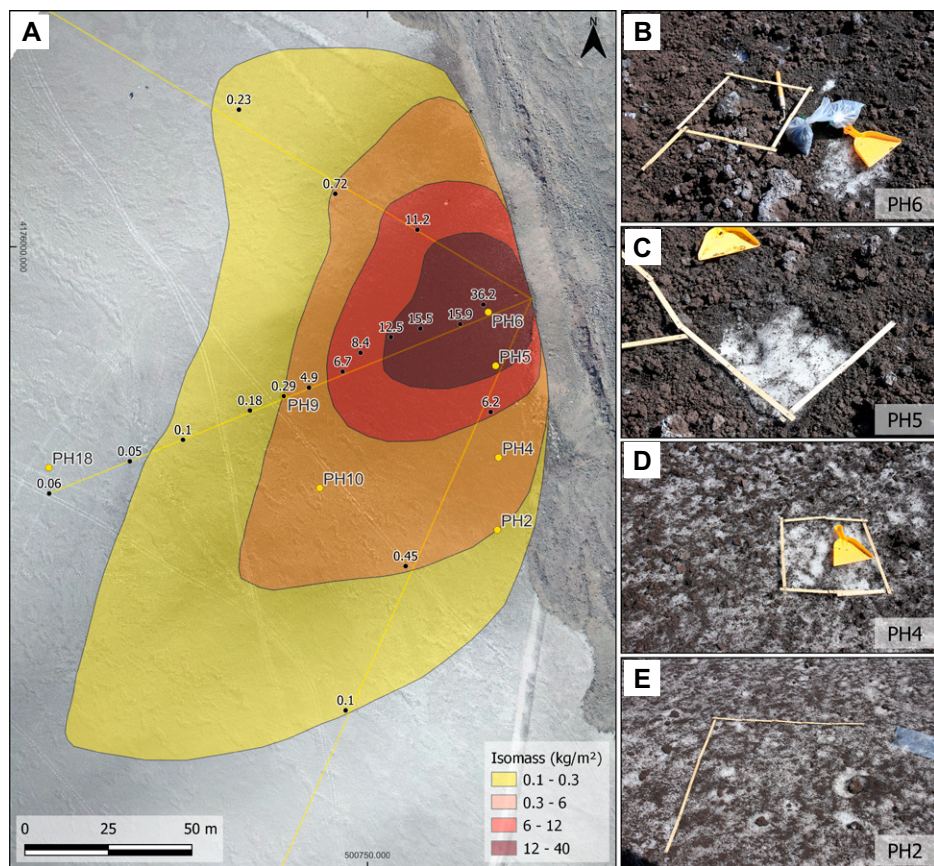


Figure 4. (A) Isomass map of the deposit; yellow dots indicate the positions of the deposit samples collected for grain-size analysis; black dots are the sites where mass loading was measured. (B) Proximal deposit with continuous clast coverage and the presence of large clasts >40 cm in diameter (locations of samples PH6 and PH7). (C) Intermediate deposit with almost continuous clast coverage (location of sample PH5). (D) Distal deposit characterized by scattered clast coverage (location of sample PH4). (E) Most distal deposit, showing a ground surface impacted by highly scattered clasts of up to 4–5 cm (locations of samples PH2 and PH3). A 2-m-long wooden folding meter is shown for scale. Photos by D. Andronico.

image analyzer (Retsch Technology; Lo Castro and Andronico, 2008). The lapilli clasts collected in the field (122 clasts, φ from -4 to -6) were divided into three different types based on their lithology, shape, and characteristics of the external surface. Clast density was measured on a subset of 83 clasts (selected from 12 samples) representative of each of the three previously defined components (Table S1). After drying and weighing, each fragment was wrapped in a plastic film and immersed in distilled water in a graduated tank to measure clast volumes by water displacement.

Nine bomb-sized clasts ($\varphi > -6$), three from each clast type, were selected for thin section preparation and vesicularity, mineral paragenesis, and groundmass texture analyses using both an optical microscope and a ZEISS EVO MA 15 scanning electron microscope (SEM) at the MEMA-UNIFI.

Component analysis was also performed on the seven samples selected for grain-size analysis, with 250 clasts randomly selected from the size classes $\varphi = -1$ and $\varphi = 0$. Additional component analyses were conducted on the finer ash fraction ($\varphi = 1$ and $\varphi = 3$) of three samples representative of the proximal, distal, and lateral portions of the deposit (PH6, PH9, and PH4, respectively; Table S1). Five different types of fine-grained components were recognized, based on the lithology, shape, and characteristics of the clasts' external surfaces.

Using the SEM, the morphological features of the different components of the ash fraction were described for a subset of 20–30 randomly picked ash particles from two different grain-size classes ($\varphi = -1$ and $\varphi = 1$) of sample PH6. Secondary electron images of the different particles were collected, the surface textures were described, and their projected shapes were

analyzed using ImageJ, an open-source software program (Schneider et al., 2012). For each particle, we calculated five shape parameters (convexity, solidity, convexity index, form factor, and elongation), as defined in Liu et al. (2015). The same particles analyzed for $\varphi = -1$ were then embedded in resin and polished, to investigate the groundmass texture of the different components after collecting digital backscattered-electron images. The crystal size distribution (CSD) of the main microlite phases was determined by first segmenting and measuring microlites with ImageJ and then performing the stereological corrections using the CSDSlice database (Morgan and Jerram, 2006) and the CSDCorrections software program (Higgins, 2000).

4. SEDIMENTOLOGICAL AND PHYSICAL CHARACTERISTICS OF THE DEPOSIT

The explosive sequence left a deposit on the ground that varied in grain-size, composed of abundant bombs scattered over a nearly continuous cover of lapilli- to ash-sized material. Aerial images from 17 March 2017 (Fig. 3B) showed a bilobate deposit flanking the western levee of lava, which is consistent with the occurrence of multiple jets from different source areas. The continuous tephra mantle (easily visible in the drone images) had an approximately elliptical shape of ~ 200 m \times 150 m, with a total area of $\sim 20,000$ m².

In general, the most striking feature of the deposit was the abundance of clasts with sizes of between 4 cm and 10 cm associated with the presence of scattered blocks with a maximum diameter of ≤ 1 m. The largest clasts were abundant in a belt within 10–20 m of the lava levee, but also episodically up to distances $> \sim 40$ m, where the deposit coverage became more erratic.

The clasts >25 cm, measured near the explosion sites (30 clasts), varied in weight from 21.2 kg to 4.8 kg (mean 9.2 kg). Most were variably fractured clinkers similar to those forming the upper crust of the lava flow. Regardless of their sizes, the largest clasts caused only occasional impact craters, possibly due to the hard, iced surface.

Different depositional facies were distinguishable in the deposit over approximately concentric areas (Fig. 4). The proximal deposit (10–20 m from the lava levee) was poorly sorted and formed a continuous mantle of ash, lapilli, and bombs (sample PH6; Table S1 and Fig. 4B). The thickness of the deposit was not consistent due to the presence of scattered blocks whose average maximum dimension ranged between 40 cm and 60 cm. Farther from the lava levee (up to 50–60

m), the deposit formed a less continuous cover on the snow (sample PH5; Table S1 and Fig. 4C), rapidly passing to an outer zone characterized by a progressively more discontinuous coverage of coarse clasts ≤ 10 cm in size (sample PH4; Table S1 and Fig. 4D). Finally, the most distal deposit (>60 m from the lava levee) consisted of highly scattered clast coverage (sample PH2; Table S1 and Fig. 4E), where the ash content significantly decreased and the frequency of the coarser clasts on the ground dropped to episodic 3–4-cm-sized clasts at a mean distance of 1–3 m apart.

The deposit was characterized in terms of mass per unit area, size, and mass of the largest clasts. Figure 5 reports the variation in the values measured along the three profiles of Figure 3B up to a distance of 200 m from the first measurement site. The mass loading measured along the three profiles shows an exponential decrease with distance, from $\sim 36 \text{ kgm}^{-2}$ to $\sim 0.06 \text{ kgm}^{-2}$. The regularity of this trend is interrupted at ~ 60 m from the explosion site, where a sharp drop in mass loading occurs, passing in a few meters from $\sim 5 \text{ kgm}^{-2}$ to $\sim 0.5 \text{ kgm}^{-2}$ (Figs. 4 and 5A). This distance corresponds to the limit between the intermediate and distal deposits, i.e., where the clast coverage becomes highly scattered (Fig. 4). Similarly, the distribution of the dimension of the three largest clasts over the whole deposit is in general well correlated with distance and shows a slowly decreasing trend starting from the explosion site (Fig. 5B). Interestingly, over the measured areas of 25 m^2 , the largest clasts (Fig. 5B) are found in the two lateral sectors rather than along the dispersal axis of the deposit, which suggests that these sectors

were more affected by low-angle, laterally ejected clasts (see below).

4.1. Ballistic Clast Dispersal and Volume

The number of blocks per unit area measured in the field was recalculated over areas of 50 m^2 at different distances from the inferred explosion vent. Results show a general exponential decrease with distance, passing from $>3 \text{ m}^{-2}$ a few meters from the lava flow to 0.2 m^{-2} at 40 m from the levee (Figs. 5C and 6).

The distribution pattern of the coarsest clasts throughout the entire field of dispersal was defined by analyzing images of georeferenced aerial photos using ImageJ software (Schneider et al., 2012; Fig. 6). Clasts larger than ~ 6.4 cm are clearly visible in the images, as they stand out above the snow cover and the ash blanket. The projected area of each block was measured and converted to an equivalent diameter. The resulting size distribution peaks at -7ϕ (both as number and vol%; Fig. 5D).

The areal frequency of the clasts >6.4 cm (Fig. 6A) clearly reflects the bilobate distribution of the deposit. Clasts >12.8 cm or >25.6 cm show a very rapid decrease in areal frequency, reaching values of 0.05 m^{-2} just a few meters beyond the lava levee (Figs. 6B and 6C). The total volume of the coarse clasts scattered on the ground was finally estimated at 5.4 m^3 by summing up the volume of each clast as calculated from the equivalent diameter (assuming the particles were spherical). Assuming an average block density of $1540 \pm 180 \text{ kgm}^{-3}$ (see Section 5.2), this value translates to a ballistic material mass of $8.4 \pm 1.0 \times 10^3 \text{ kg}$.

4.2. Mass and Volume of the Total Deposit

The mass of material involved in the explosions (excluding the coarsest clasts) was calculated by tracing four isomass curves of the deposit (Fig. 4A) and integrating the values obtained with two different methods (exponential thinning and trapezoidal rule; Pyle, 1989; Fierstein and Nathenson, 1992), which resulted in an average value of the estimated deposit mass of $5.8 \pm 0.7 \times 10^4 \text{ kg}$. This value, summed up to the mass of the ballistic blocks, resulted in a total mass of $7.1 \pm 0.8 \times 10^4 \text{ kg}$ for the ejected material. Assuming a lava flow density of $\sim 2200 \text{ kgm}^{-3}$ (an averaged value between that of the crust and massive portions of the lava flow), the volume of lava involved in the explosive sequence is $32.0 \pm 3.6 \text{ m}^3$. Given the observed average thickness of the lava flow, which is $\sim 2.5 \pm 0.5 \text{ m}$ at the front and along the southern lava levee (Fig. 1C), the material ejected in the explosion can be reconciled with an excavated cylinder of $\sim 4.0 \pm 0.6 \text{ m}$ in diameter or, alternatively, with a rootless crater of conical shape with a downward vertex and an upper diameter of $\sim 7.0 \pm 1.1 \text{ m}$.

4.3. Grain Size

Due to the marked heterogeneity of the deposit, grain-size analyses were performed on samples from seven sites at different positions inside the dispersal fan. Grain-size distributions are highly irregular, varying from unimodal and strongly positively skewed (e.g., samples PH4, PH5, and PH6; Fig. 7) to multimodal distributions (e.g., sample PH 9; Fig. 7). In many cases, the grain-size distribution is discontinuous, with gaps between different grain-

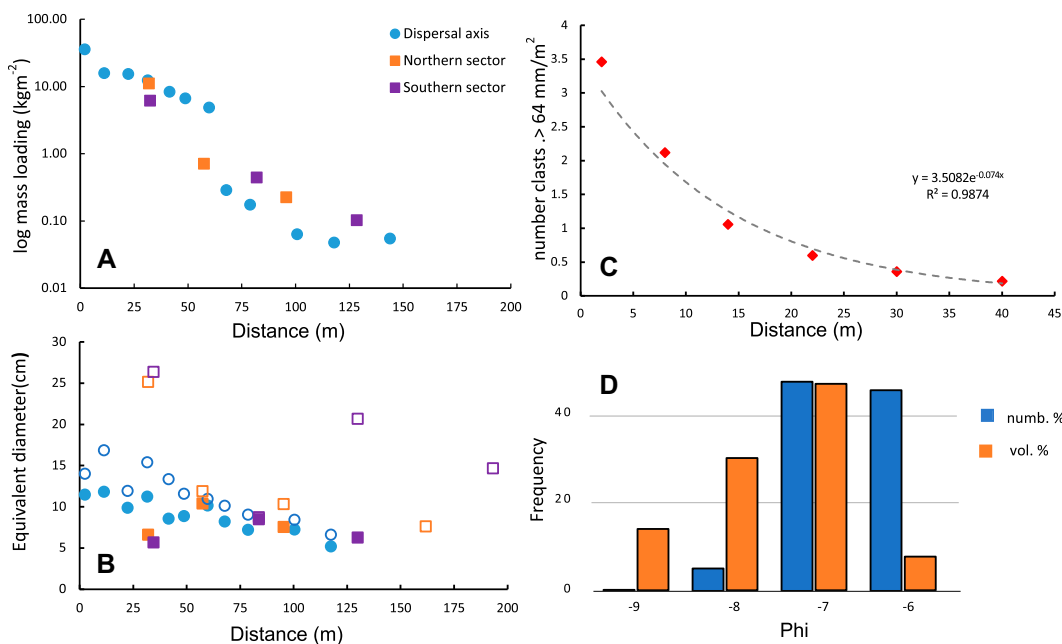


Figure 5. (A) Logarithm of mass loading versus distance from the lava levee measured along the three profiles shown in Figure 3B. (B) Equivalent diameter of the average value of the three maximum clasts (full symbols) and of the maximum clast (open symbols) versus distance from the lava flow. Colors are as in panel A. (C) Number of coarse clasts per unit area versus distance measured along the dispersal axis. (D) Grain size of the coarse material as measured by analyzing aerial photos, in terms of frequency (number and vol%).

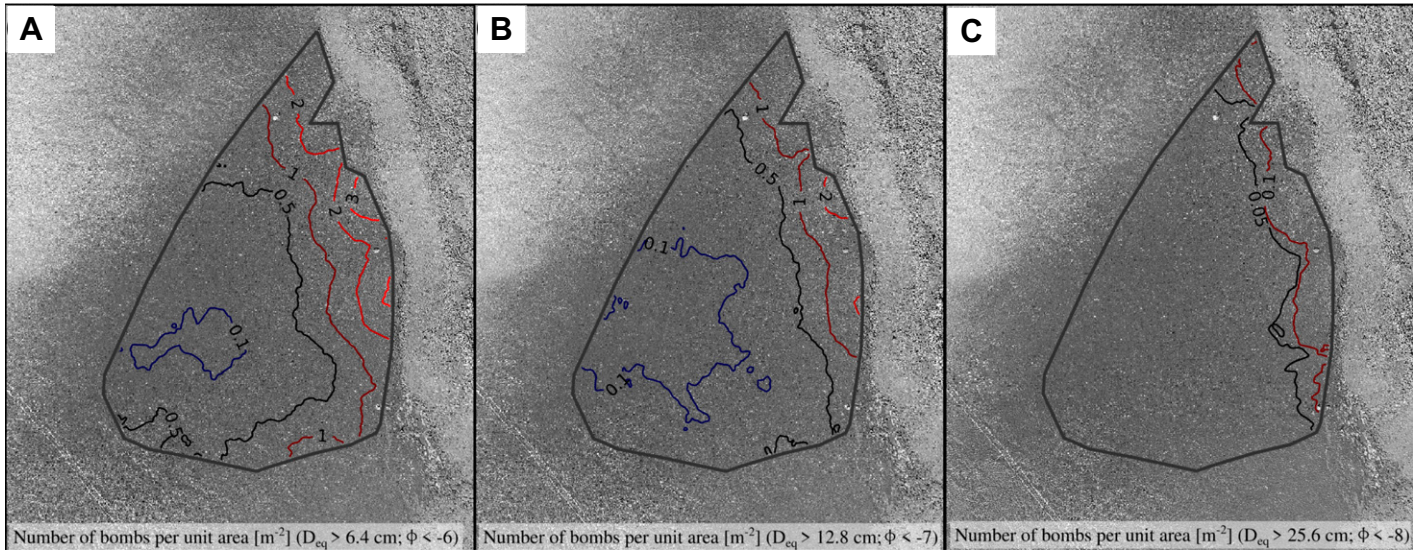


Figure 6. Number of bombs per unit area of the deposit studied, with different block dimensions shown.

sizes. The amount of ash increases with distance from the explosion site, although its distribution is irregular and, in the lateral portions of the dispersal fan (at <30 m from the main dispersal axis), ash is scarce. Fine ash ($>4\varphi$) is, however, very poor or absent throughout the deposit (Fig. 7).

Grain-size data from different sites were integrated by averaging the grain-size distribution of samples over the area of the corresponding iso-mass to obtain an integrated grain-size distribution of the deposit. To obtain the cumulative total grain-size distribution (TGSD) of the material ejected during the different explosions (Fig. 7C), block-sized clast data (Fig. 5D) were recalculated by normalizing the total mass of ballistic blocks to the total mass of the deposit and added to the integrated grain-size distribution of the deposit. TGSD is slightly asymmetric and bimodal: it presents a

major mode at $\varphi = -6$ and a secondary mode at $\varphi = 1$. In total, the ash material is no more than 8 wt%, with nearly no fine ash ($\varphi > 4$). We highlight that the TGSD described is associated with a pyroclastic deposit that includes material from a series of explosions that involved different portions of a heterogeneous lava flow, despite occurring closely spaced in time and distance and being likely dominated by the largest explosion.

5. ANALYSIS OF THE EJECTED MATERIAL

Further analyses of componentry, morphology, textural features, and density of the ejected material were conducted separately on coarse and fine material, which here are arbitrarily defined as clasts with diameters of $\leq -4\varphi$

and $\geq -3\varphi$, respectively. These two groups represent 65 wt% and 35 wt% of the total ejected material. Due to the different scale of details recognized on coarse (visual) and fine material (microscopy), we distinguished several types of fragments that can all be correlated with the different portions of the lava flow.

5.1. Componentry of the Coarse Material

The componentry of coarse material was determined for 355 clasts >32 mm in diameter collected from 10 different sites. They were measured and divided into three types based on their morphological and lithological features (Fig. S2).

(1) Poorly vesicular (PV) clasts (Fig. S2A) are gray to dark brown fragments with irregular, sub-rounded to blocky shapes and largely irregular

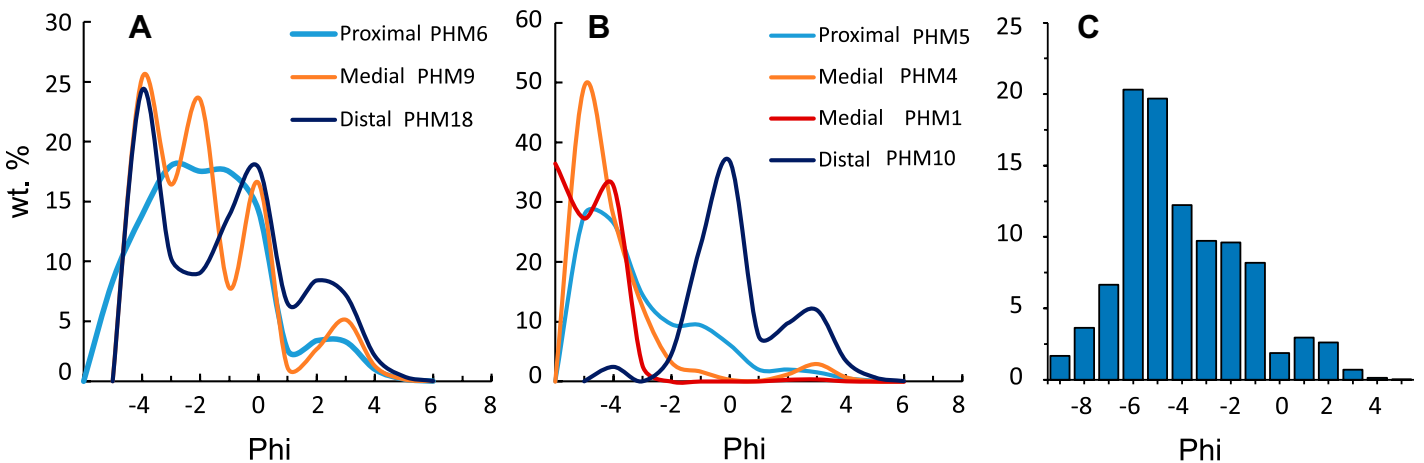


Figure 7. Grain-size distributions of samples collected along (A) the main dispersal axis and (B) along the southernmost transversal transect shown in Figure 3B. (C) Total grain-size distribution of the deposit, in wt%.

spiny surfaces that are sometimes altered. They represent ~60 wt% of all of the measured clasts.

(2) Scoriaceous, vesicular (SV) clasts (Fig. S2B) are gray to orange-brown, irregularly shaped fragments. Surfaces vary from spongy to smooth and are characterized by abundant vesicles that vary greatly in size and are easily visible on the external surfaces as well, making them easier to distinguish from PVs. They represent ~35 wt% of the total coarse material.

(3) Glassy (G) clasts (Fig. S2C) are black scoria clasts that often show a metallic luster. They have very irregular and spiny shapes and poor external vesicularity. Their percentage varies largely from sample to sample, and they are more abundant at sites closer to the lava flow. On average, they represent 5 wt% of the coarse material.

5.2. Density of the Coarse Material

The density of the different types of coarse material was measured on 83 clasts in the 16–64 mm range (Fig. S4). Density values range between 970 kgm^{-3} and 2110 kgm^{-3} and differ greatly among the three different types of clasts, passing from an average value of $1190 \pm 190 \text{ kgm}^{-3}$ for the G clasts to $1400 \pm 160 \text{ kgm}^{-3}$ for the SV clasts, up to the value of $1660 \pm 180 \text{ kgm}^{-3}$ typical of PV clasts. While the distribution of SV density is unimodal and nearly symmetric, distribution of PV density is bimodal, with the primary and secondary modes being positioned around 1800 kgm^{-3} and 1600 kgm^{-3} , respectively. The density value of the material studied, averaged over all of the different types of clasts and weighed by the relative abundance of each type, is $1540 \pm 180 \text{ kgm}^{-3}$.

5.3. Componentry of Fine Material

Analysis of fine-grained material (Fig. 8) reveals a larger lithological variability with respect to the coarse material, which possibly better represents the general textural inhomogeneity of the products studied. Fine clasts were split into five different types, in addition to loose crystals. Surface features of each type were described for clasts in the -1φ and 1φ classes using an SEM at MEMA-UNIFI.

(1) Altered clasts (ALT) consist of brownish-orange, superficially oxidized fragments with a scoria-like surface and irregular to subrounded, oblate shapes (Figs. 8, 9A, and 9B). Microlites of pyroxene and Fe-Ti oxides are disseminated on the external surface, along with fragments of fine ash. Surface cracks are often present, especially on coarse ash. ALT generally represent the most abundant class (average 38 wt%).

(2) Glassy clasts (GLY) are light gray to black, with irregular to subrounded shapes and shiny

surfaces (Figs. 8, 9C, and 9D). The external surface locally shows smooth glassy regions or very rough zones formed by pyroxene (with hollow shapes) and oxide microlites protruding from the groundmass. GLY particles are significantly more abundant in the 0φ and -1φ classes, with a mean value of 24 wt% for all of the analyzed classes.

(3) Fluidal clasts (FLU) are represented by glassy, typically amber-colored fragments that are highly irregular in shape (this type includes fluidal, stretched, and convoluted shapes as well as episodic Pele's hair; Figs. 8, 9E, and 9F). Clasts have vesicles of variable dimensions. The typical smooth, glassy external surface rarely has microlites or aggregated fine ash. Quench fractures are present on the surface. FLU are generally $<10 \text{ wt%}$ in the different samples, and only 5 wt% on average.

(4) Blocky clasts (BLK) are composed of dense, subangular fragments, with internal black glassy portions and shiny conchoidal fractures. The external surface is formed by plane-to-concave surfaces that are suggestive of rigid fracture planes, with rare protruding microlites (Figs. 8, 9G, and 9H). BLK predominate in the finer-grained material (1φ and 3φ classes), and represent ~22 wt% of the deposit.

(5) Vesicular clasts (VES) are formed by brownish to gray-colored, irregularly shaped particles that are characterized by opaque, smooth to mildly rough surfaces, and by isolated, sparse vesicles of up to $100 \mu\text{m}$ in size in the groundmass. External surfaces mainly display a complex intersection of the inner walls of large vesicles (Figs. 8, 9J, and 9H). VES never represent $>18\%$ of the total amount of each class analyzed and generally comprise $<10\%$ (average 9 wt%).

(6) Loose crystals include crystals or fragments of plagioclase, pyroxene, and subordinate olivine. Free crystals form up to 20% of the 3φ class (Fig. 8, green bars), are very scarce or absent in coarser classes, and total $<2 \text{ wt%}$ of the fraction of lapilli/ash.

5.4. Ash Morphology

The morphology of ash-sized material was characterized using selected parameters calculated based on the apparent 2-D projected shapes of randomly picked grains from all of the different clast types (crystals excluded) for two size classes (-1φ and 1φ ; Figs. 10 and S3, respectively). Shape parameters of particles from different samples show very limited variability, while differences can be observed between the different types of clasts. FLU, and less frequently GLY and VES, fragments present the lowest values of solidity and convexity (Fig. 10A) and reflect a more complex projected shape mainly because of the presence of a diffuse micro-vesicularity in

these clasts. Similarly, the highest values of concavity index (which suggest complex morphologies) are again shown by FLU, GLY, and VES fragments (Fig. 10B). Data collected on clasts of the -1φ and 1φ classes show similar distributions of shape parameters, which suggests a general invariance with size, at least in the coarse ash fraction (Figs. 10 and S3, respectively). The observed low values of solidity (<0.6), convexity (<0.65), and form factor (<0.2) are uncommon in pyroclastic materials related to primary explosive activity (Hantusch et al., 2021; Leibbrandt and Le Pennec, 2015) and reflect the presence of largely irregular and convoluted particles.

5.5. Textural Parameters of Ash Groundmass

The relations between the three classes of coarse material (Section 5.1) and the five types of fine material components (Section 5.3) can be proposed based mainly on the characteristics of the external morphologies, the petrographic features, and the groundmass textures (Fig. 11). On this basis, the VES and some of the BLK fragments are similar to the PV scoria, the ALT and some of the BLK are similar to the SV fragments, and the GLY and FLU are similar to the G fragments (Fig. 11).

The groundmass texture of the ash fragments produced by the explosion records important differences that can be related to the dynamics of lava emplacement and, possibly, to the mechanisms of explosive fragmentation. Glass is measurably present in GLY and, more abundantly, in FLU (Table 1 and Fig. 11). Conversely, in the ALT, VES, and BLK, the groundmass is almost completely crystallized (Table 1). Plagioclase always has an acicular habit (Table 1), and the dimensional ratio is similar for all of the clast types except for GLY, for which plagioclase is slightly less elongated (Table 1). Groundmass in the SV, ALT, and part of the BLK fragments is also characterized by an abundance of tiny ($<5 \mu\text{m}$) oxides generally bordering microlites and microphenocrysts, which are similar to those described by D'Orlando et al. (2014) for thermally recycled clasts (Fig. 11).

Plagioclase is always the largest mineral, with a volume-based dominant size ($3G\tau$; Marsh, 1988) of the different types of clasts typically ranging from $40 \mu\text{m}$ to $100 \mu\text{m}$ (Figs. 12, 13A, and 13B). GLY have smaller plagioclase microlites in a very limited dimensional range ($<100 \mu\text{m}$; Fig. 13B). Values of N_v (volumetric number density) show little variability (Table 1; Fig. 13).

Mafic groundmass minerals (mainly clinopyroxene and olivine) are instead very fine-grained ($3G\tau$ from $10 \mu\text{m}$ to $20 \mu\text{m}$; Fig. 12) and have a highly variable N_v value, reaching the maximum

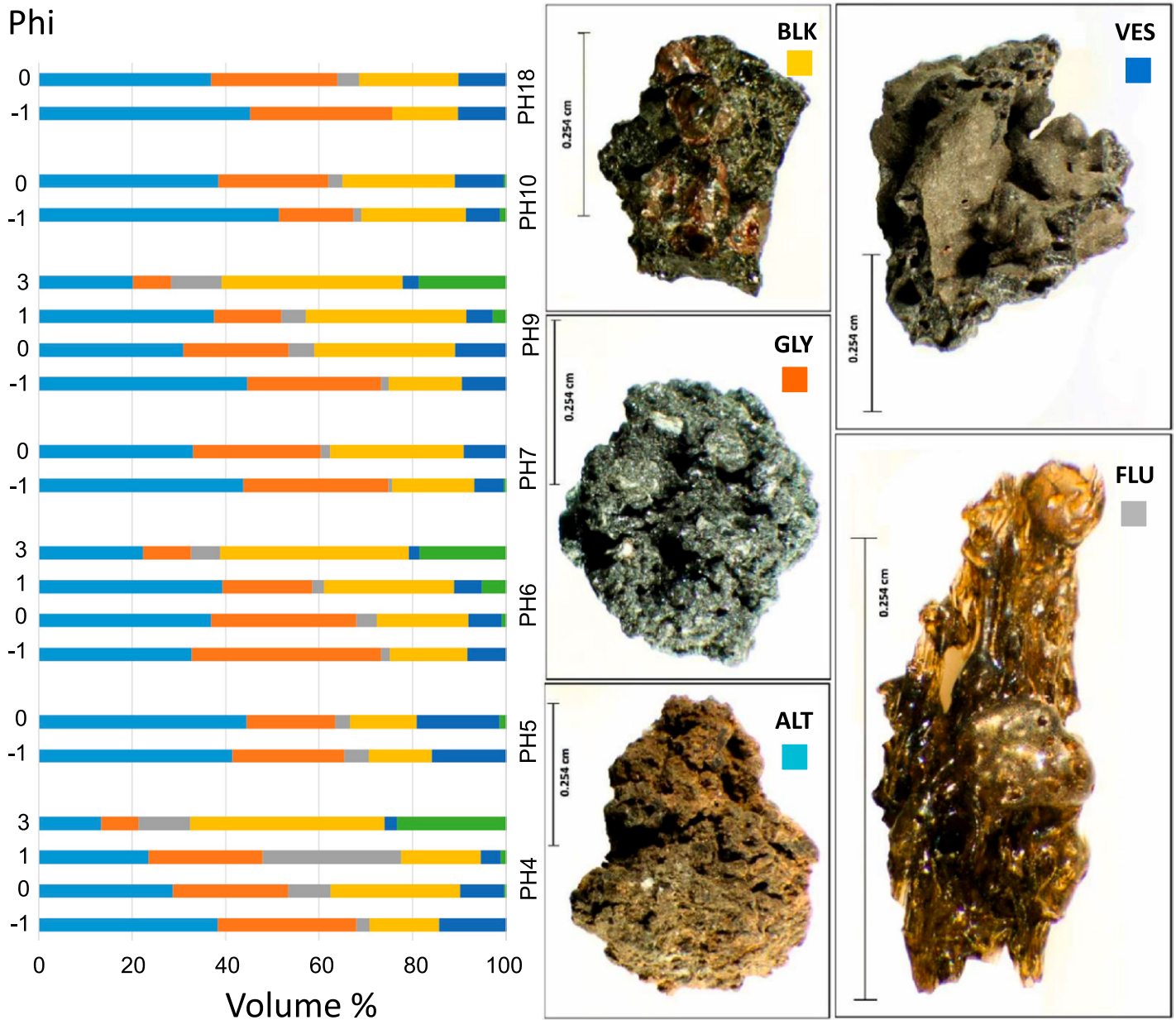


Figure 8. Componentry of fine-grained material of different samples, with grain-size classes ranging from $\phi = -1$ to $\phi = 3$ (Table S1 [see text footnote 1] shows sample locations). Bar colors correspond to the colored squares shown next to the images of the different components.

value for GLY (Table 1 and Fig. 12). Mafic minerals from all of the clast types have very similar, prismatic, poorly elongated shapes (Table 1) and a similar size distribution (Figs. 13C and 13D).

While glass progressively decreases from the FLU through GLY, VES, BLK, and ALT, a similar continuous change in the other textural parameters is not evident (Figs. 12 and 13; Table 1). FLU are characterized by the lowest N_V (both for plagioclase or feric minerals) and the largest plagioclase microlites. Conversely, GLY have the smallest microlites (in terms of dominant size) and the largest N_V values of the mafic minerals.

The CSD curves of the GLY show the highest slope (smaller size) both for plagioclase and mafic minerals (Table 1 and Fig. 13A). Conversely, FLU show high slopes for both plagioclase and mafic minerals (Table 1; Figs. 13A and 13C), and they are also characterized by the lowest values of n_0 (Table 1).

6. LAUNCH VELOCITY AND KINETIC ENERGY OF BALLISTIC CLASTS

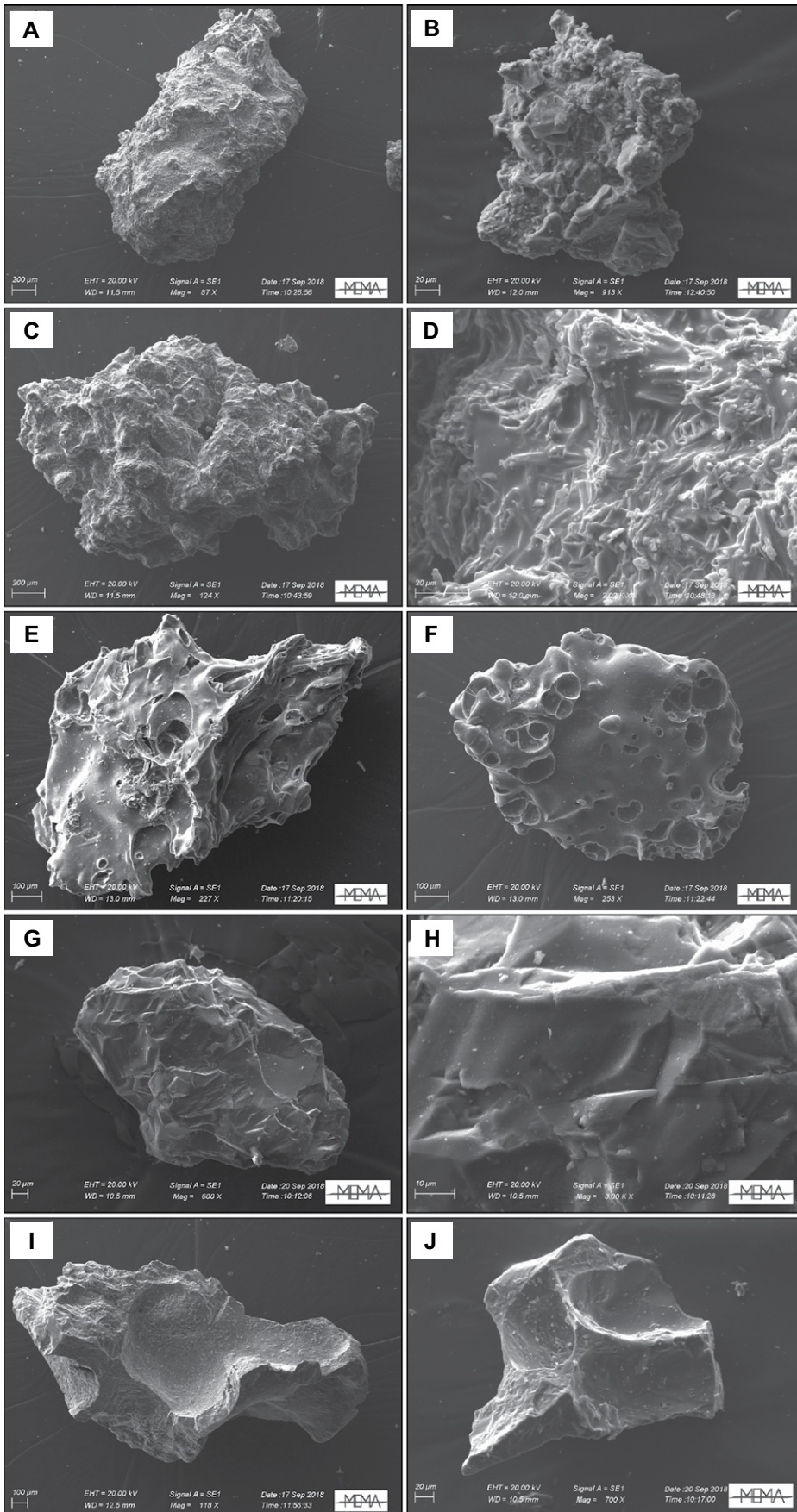
We adopted an inverse modeling strategy to constrain the launch conditions of the ballistic

clasts using the Eject! program (Mastin, 2001). Note, however, that different sources of uncertainty are recognized in the characteristics of the explosions studied, and thus some simplifications are needed to perform numerical simulations. Accordingly, our numerical results should be intended as a first-order approximation. Since the available video footage shows the occurrence of multiple explosions sourced from sites dispersed within a fairly limited area, the position of the vent site was considered to be fixed in our calculations, while clasts were approximated as spheres to compute the drag force during

Figure 9. Representative scanning electron microscope (SEM) secondary electron images of the different components recognized in the fine material. (A and B) Altered clasts (ALT). (C and D) Glassy clasts (GLY), with image in part D showing detail on the smooth surface made rough by shallow crystals. (E and F) Fluidal clasts (FLU). (G and H) Blocky clasts (BLK), with image in part H showing detail on smooth surfaces, and cut parallel planes. (I and J) Vesicular clasts (VES). See text for descriptions.



the ballistic trajectory. With these assumptions, measures of dimension, density, and distance from the lava flow can be used to estimate variation ranges for the launch velocity and kinetic energy per unit surface needed to reach the position where the blocks were sampled, which are functions of the launch angle (Fig. 14). Launch velocity estimates for the blocks with D_{eq} larger than 20 cm collected in the vicinity of the lava flow (distance between 6 m and 14 m) range between 10 ms^{-1} and 20 ms^{-1} , which is a remarkably narrow variation range considering that these results are associated with simulations with highly variable values of launch angle ranging from 15° to 75° . Higher launch velocities of between $\sim 30 \text{ ms}^{-1}$ and $\sim 60 \text{ ms}^{-1}$ were computed for slightly smaller clasts (D_{eq} of 5.8–10.5 cm) from samples PH13, PH15, PH16, and PH19, which were collected at distances of $\sim 70 \text{ m}$, $\sim 80 \text{ m}$, $\sim 100 \text{ m}$, and $\sim 145 \text{ m}$ from the lava flow, respectively (Fig. 14A). If we assume that the energy transfer from the expanding gas to the ejected pyroclasts is proportional to the external surface of the solid material, the kinetic energy per unit surface can be considered as an informative measure for understanding the dynamics of block acceleration (Fig. 14B). The significant gap between proximal large blocks and the small blocks scattered at distal sites (i.e., PH13, PH15, PH16, and PH19), which is evident in the plots of launch velocity, is not recognized when we consider the kinetic energy per unit surface, as a more continuous transition is observed. This transition goes from large blocks with relatively less efficient energy transfer (kinetic energy per unit surface $< 20,000 \text{ kgs}^{-2}$; Fig. 14B) to smaller blocks subject to more efficient energy transfer (kinetic energy per unit surface from $\sim 15,000 \text{ kgs}^{-2}$ to $> 50,000 \text{ kgs}^{-2}$; Fig. 14B). The average landing velocities of the blocks measured at different distances vary between 15 ms^{-1} and 30 ms^{-1} , which corresponds to impact energies of between 100 J and 250 J and impact energy densities (impact energy divided by cross-sectional area of the clast) of between 3 Jmm^{-2} and 6 Jmm^{-2} .



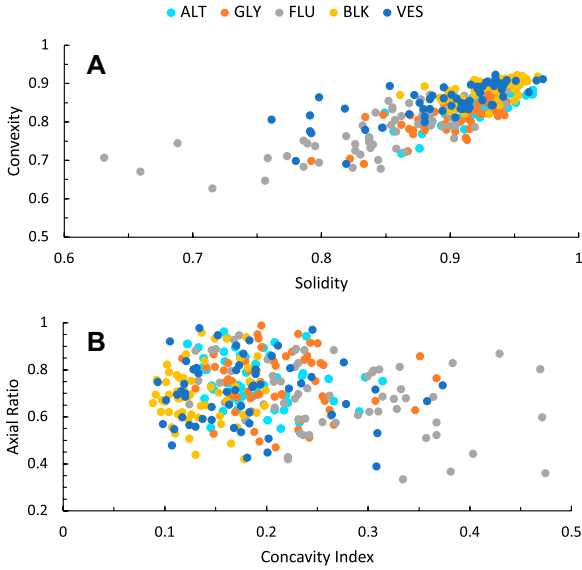


Figure 10. Shape parameters (Liu et al., 2015) for the samples PH4, PH6, and PH9 related to the grain-size class $\phi = -1$. (A) Solidity versus convexity; (B) concavity index versus axial ratio. ALT—altered clasts; BLK—blocky clasts; FLU—fluidal clasts; GLY—glassy clasts; VES—vesicular clasts.

7. DISCUSSION

Explosions triggered by the sudden vaporization of ice/snow during lava flow effusions are small and ephemeral events, but possibly frequent (Belousov et al., 2011; Edwards et al., 2012, 2013, 2015). Nonetheless, while many of these events have been observed directly worldwide or their deposits have been recognized by remote sensing analysis of volcanic terrains on Earth and other planets (Belousov et al., 2011; Dundas and Keszthelyi, 2013; Edwards et al., 2014, 2015; Conway et al., 2015), a complete study of their products has not, to our knowledge, ever been presented before. In fact, the general low energy (in respect to a common volcanic scale) associated with these explosions determines the formation of small-volume, poorly dispersed deposits with a low preservation potential. Where these deposits are

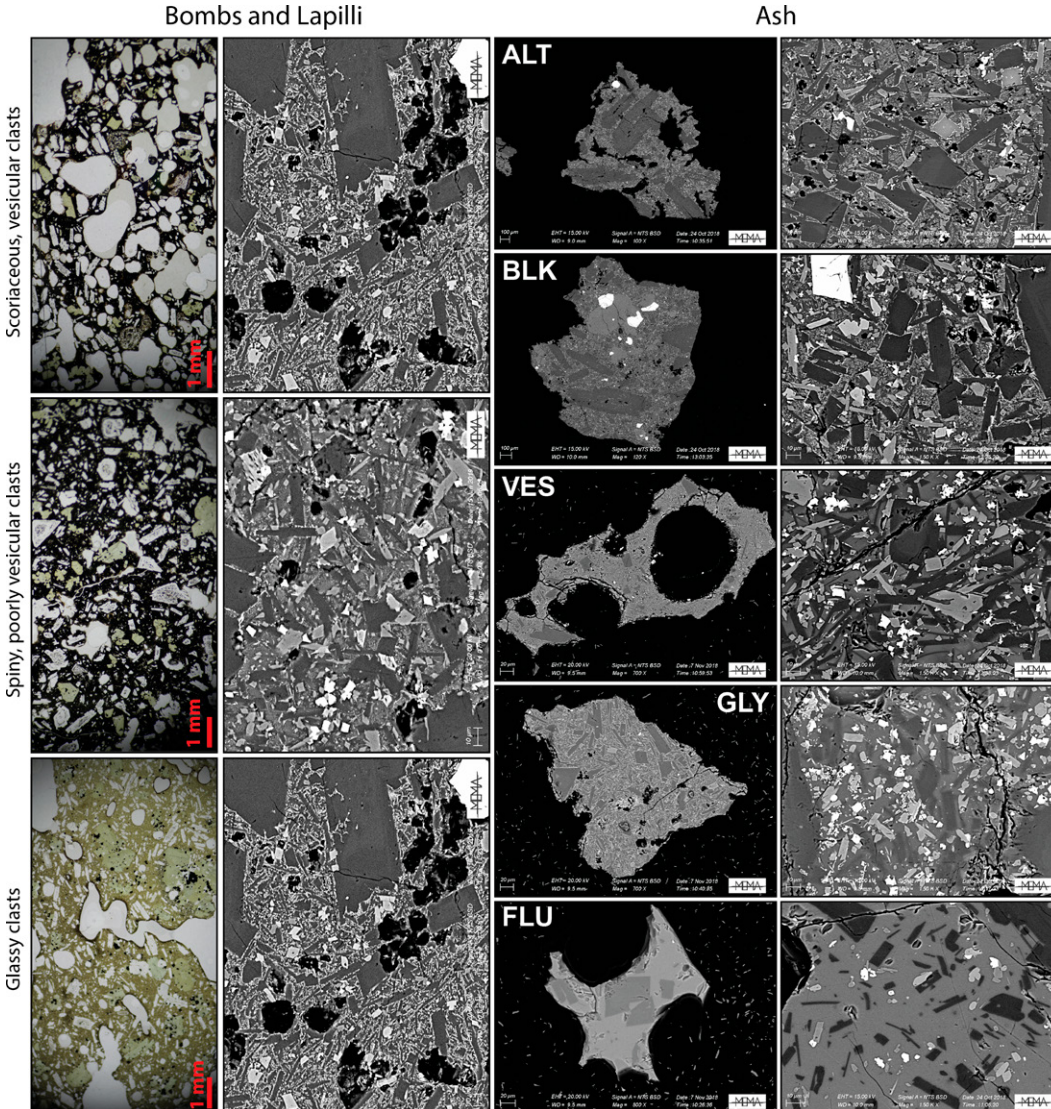


Figure 11. Mosaic of optical microscope images of the different lithologies/morphologies in the coarse clasts (bombs and lapilli) and scanning electron microscope (SEM) images of the fine material (ash). See text for explanation. In particular, for bombs and lapilli, the left column shows a transmitted light image, and the right column shows a backscattered SEM image of the same clast. For ash, the left column shows images of single particles, while the right column shows a magnification of the texture. ALT—altered clasts; GLY—glassy clasts; FLU—fluidal clasts; BLK—blocky clasts; VES—vesicular clasts.

TABLE 1. GROUNDMASS DATA (PLAGIOCLASE AND CLINOPYROXENE) AS DERIVED FROM IMAGE ANALYSIS OF THE DIFFERENT CLAST TYPES

Clast type	ALT	GLY	FLU	BLK	VES
Plagioclase					
N_A (mm^{-2})	$4.58 \cdot 10^3$	$2.21 \cdot 10^3$	$3.07 \cdot 10^3$	$4.76 \cdot 10^3$	$6.17 \cdot 10^3$
N_V (mm^{-3})	$2.78 \cdot 10^5$	$2.02 \cdot 10^5$	$1.51 \cdot 10^5$	$4.01 \cdot 10^5$	$3.64 \cdot 10^5$
n_0 (mm^{-4})	16.32	16.45	15.38	16.52	16.61
$1/G_\tau$ (μm^{-1})	0.044	0.069	0.032	0.038	0.045
$3G_\tau$ (μm)	68.0	43.2	94.9	80.0	67.0
vol%	66.5 ± 12.8	28.5 ± 6.0	43.1 ± 10.6	59.3 ± 12.3	61.0 ± 11.4
Shape x:y:z	1.0:3.0:10.0	1.0:2.9:6.0	1.0:1.5:10.0	1.0:3.0:10.0	1.0:3.6:10.0
Mafic minerals					
N_A (mm^{-2})	$8.69 \cdot 10^3$	$1.55 \cdot 10^4$	$3.07 \cdot 10^3$	$1.38 \cdot 10^4$	$5.77 \cdot 10^3$
N_V (mm^{-3})	$1.71 \cdot 10^6$	$3.55 \cdot 10^6$	$5.59 \cdot 10^5$	$2.53 \cdot 10^6$	$7.64 \cdot 10^5$
n_0 (mm^{-4})	19.61	20.48	18.29	19.88	18.36
$1/G_\tau$ (μm^{-1})	0.193	0.222	0.157	0.170	0.123
$3G_\tau$ (μm)	15.5	13.5	19.1	17.6	24.4
vol%	28.0 ± 4.7	35.5 ± 4.8	11.4 ± 3.0	33.7 ± 4.9	24.0 ± 4.6
Shape x:y:z	1.0:1.2:2.1	1.0:1.3:2.1	1.0:1.4:2.8	1.0:1.4:2.8	1.0:1.3:3.2
Glass					
vol%		36.0 ± 10.8	45.5 ± 13.6		15.0 ± 16.0

Note: ALT—altered clasts; GLY—glassy clasts; FLU—fluidal clasts; BLK—blocky clasts; VES—vesicular clasts; N_A —number of crystals per unit area; N_V —number of crystals per unit volume; n_0 —nucleation density; G —growth rate; τ —residence time. Shape indexes (x, y, z) were estimated using the CSDSlice database (Morgan and Jerram, 2006).

preserved, they are difficult to recognize in the field. However, a good definition of the conditions that lead to these events and the dynamics of their occurrence is important to determine, as they can be very high risk, especially at active volcanoes visited by tourists. In the following section, we discuss the mechanisms responsible for the sequence of explosions studied (Section 7.1) and then propose a reconstruction of the internal structure of an ongoing lava flow based on the information derived from the different components of the deposit (Section 7.2). Lastly, we comment on the dynamics of the explosions (Section 7.3).

7.1. Mechanisms of Lava-Snow/Ice Explosion

Mechanisms of lava-snow/ice interaction have been widely debated mainly in relation to littoral cone formation or for subglacial or supraglacial activity in terrestrial or extraterrestrial environments. Similarly, lava-water contact in

lacustrine, swampy, or marine environments has been discussed by many authors (e.g., Mattox and Mangan, 1997; Hamilton et al., 2010; Fitch et al., 2017). Fagents and Thordarson (2007) first reviewed the different mechanisms suggested for this type of explosion, proposing two different models: a static heat transfer model and a dynamic heat transfer model.

Pressure build-up by vapor generation below the lava flow represents the base of the static heat transfer model (Thorarinsson, 1953). It is controlled by the thermal coupling between the lava flow and the snow and by the characteristics of the basal surface and the internal permeability of the lava, which may prevent or favor vapor escape. In the case of an active lava flow, permeability can be reduced by the presence of a melt layer in the inner part of the lava flow. In this model, some characteristics of the substratum, such as low permeability and the presence of small local depressions below the lava, may produce the most favorable conditions for accumulating vapor and triggering an explosion.

The extent of the overpressure needed to drive an explosion is closely defined by the thickness and density of the lava flow, by the tensile strength of its rigid portion, and by the yield strength of its melted core. For the 16 March 2017 lava flow, this variable can be calculated at ~ 1 – 10 MPa, and it is mainly controlled by the tensile strength of the upper crust (Lyman et al., 2005). The main parameters controlling the thermodynamics of the static model are the effective thermal coupling of lava and ice/snow (which depends upon whether a basal scoria layer is present or not), the ice/snow permeability (which controls the possibility of water drainage toward areas beyond or underneath the lava flow), and the thickness of the lava and the ice/snow cover (Wilson and Head, 2007; Edwards et al., 2015). The rate of ice/snow melting is directly related to the temperature and thickness of the lava. For instance, Wilson and Head (2007) clearly demonstrated that thinner lava flows result in more rapid (though briefer) heat transfer to the substratum. By means of analytical thermal models that can describe the interaction between lava flows and ice, they simulated rates of ice melting of $20 \mu\text{m s}^{-1}$ and $10 \mu\text{m s}^{-1}$ during the first 4 h and 16 h, respectively, from the arrival of a lava flow of ~ 1 – 3 m thickness. This means that ice varying in thickness from 30 cm to 60 cm could have melted in a few hours, and large amounts of water could easily accumulate in small depressions underneath the lava flow as water migrated from the more elevated surrounding areas. Water percolation through the ice/snow cover was directly observed by Edwards et al. (2015) in front of a lava flow at Tolbachick volcano. The vaporization of water ponds below the lava could then sustain the explosions. The heat transfer from the lava to the substratum could even be greater with respect to that calculated by Wil-

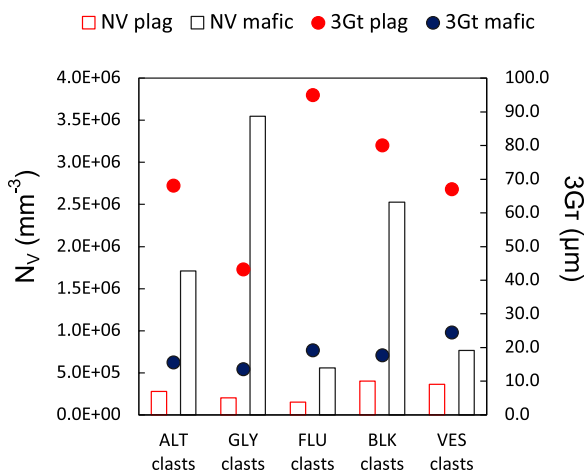


Figure 12. Main textural parameters for the minerals (pl—plagioclase; mafic—olivine and clinopyroxene) present in the groundmass of the different fine-grained components. N_V —volumetric number density; ALT—altered clasts; GLY—glassy clasts; FLU—fluidal clasts; BLK—blocky clasts; VES—vesicular clasts.

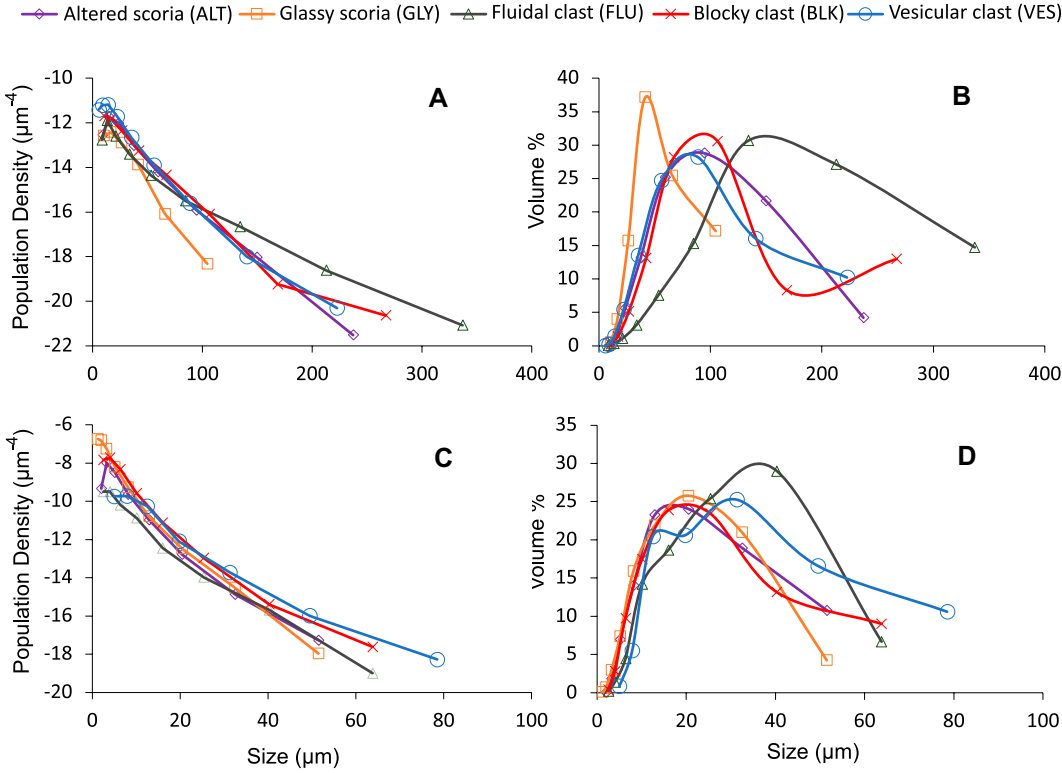


Figure 13. Diagrams of population density and volume size distribution for (A, B) plagioclase and (C, D) mafic microlites from the groundmass of the different fine-grained components.

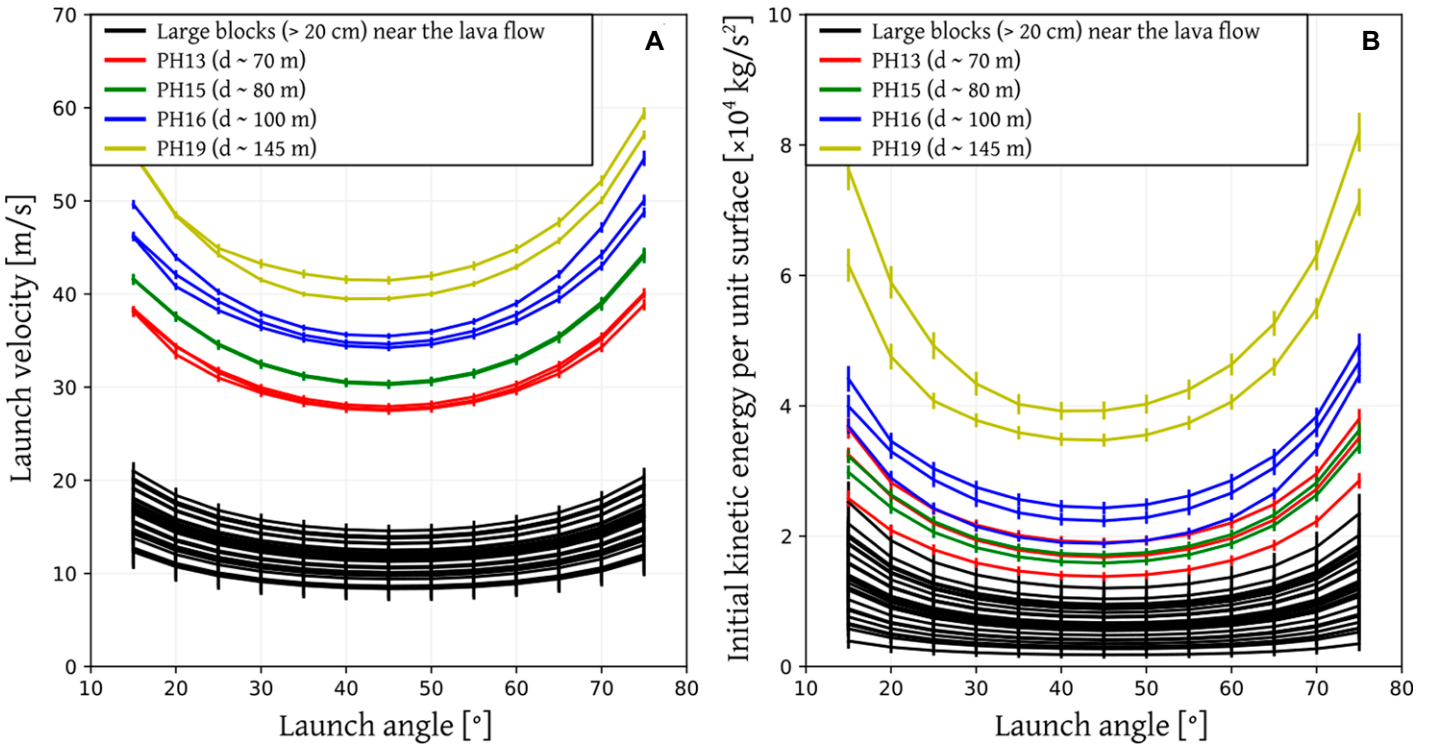


Figure 14. (A) Launch velocity and (B) initial kinetic energy per unit surface as a function of launch angle for a set of blocks collected near the lava flow and for samples PH13, PH15, PH16, and PH19 (see legend). Results were computed using Eject! (Mastin, 2001), with our measures of dimensions, density, and distance from the lava flow for each block as input data. Error bars were computed by introducing an uncertainty of 5% in all of the data.

son and Head (2007) in the case of fast-moving flows and due to the effect of latent heat release during lava crystallization. The textural features of the different types of clasts recognized in the eruption, with a variable crystallinity of between ~50 wt% and >90 wt% (Table 1), suggest a significant contribution of latent heat (that could be approximated as a rise in temperature on the order of 180–300 °C; Couch et al., 2001; Blundy et al., 2006) to the total heat transfer (an additional 20%–30%).

Different from the static model, the dynamic heat transfer model (Fagents and Thordarson, 2007) involves a mechanism of melt fuel-coolant interaction (MFCI; Wohletz, 1986; Zimanowski et al., 2015), which is triggered by mixing of the lava with a slurry of snow, water, and soil, possibly resulting from the drag at the base of the lava flow. Intimate mixing results in more efficient heat transfer compared to simple conduction, inducing sudden vaporization of the snow–water–ice slurry with the consequent trigger of an explosion. The efficiency of the interaction depends on many factors (magma/water ratio, fluidity, and temperature of the interacting lava portions), and many authors have discussed this in terms of the textural features of the ash formed during the explosion. Fitch and Fagents (2020), studying the deposits of the Pu'u Kīlolo rootless cone in Hawaii, discussed the mechanisms of cone formation in terms of MFCI, recognizing ash fragments that possibly formed at the magma-water contact and were mainly characterized by mossy to blocky shapes and glassy to partially crystallized groundmasses. MFCI was invoked as a mechanism to explain the prolonged sequence of explosions that characterizes the formation of rootless cones. Despite this, MFCI processes could only have become dominant after the initial formation of a crater for static vapor accumulation, facilitating the free access of fluid, molten lava to water or snow, during the ensuing activity (Fagents and Thordarson, 2007; Fagents et al., 2002; Fitch and Fagents, 2020). The data collected for the different types of fragments from the 16 March 2017 explosion at Etna can be used to discuss the event dynamics in terms of one of the two different models. Coarse clasts are dominated by highly crystallized vesicular and poorly vesicular types, with only a minor proportion of glassy clasts. The external surface of these fragments is irregular, and there is no clear evidence of quenching textures or fractures (e.g., glassy rinds, marked vesicularity gradients, or cooling-induced jointing). All of these features are typical of fragments derived from the external, partially cooled portions of the aa lava flow, which are dominated by scoriaceous material that did not interact directly with the snow. The

estimated volume of ejected block-sized material (~5 m³) is compatible with the disruption of a thin (generally <1 m, for basaltic lava flows) upper scoriaceous cap of the lava flow, which is removed during the explosion from a crater only a few meters in diameter (between 4 m and 7 m, as derived from the estimated volume of the total ejected material). Conversely, the fine-grained clasts have textural and morphological features that are clearly transitional from glass-bearing, poorly crystallized material to holocrystalline, externally altered, glass-free clasts, which are probably derived preferentially from fragmentation of the internal and basal portions of the lava flow. Fine ash, the typical product of MFCI, is instead nearly absent from the deposit (much less than 1%; Fig. 7C). Again, SEM analysis of the different types of clasts does not show any clear evidence of important hydromagmatic fragmentation, such as surface quench fractures, significant aggregation of cohesive wet ash over the grains, or mossy surfaces derived by particles annealing after fragmentation (e.g., Heiken et al., 1988; Cioni et al., 1992; Büttner et al., 1999; Zimanowski et al., 2015). The variability of the microlites in the groundmass of ash fragments is clearly continuous, as demonstrated by the variable size and N_v of plagioclase shown in CSDs, which confirms the provenance of these clasts being the shattering of the entire thickness of the lava body during the explosion, as is expected for an explosion triggered by water vaporization underneath the lava flow (see Section 7.2). Furthermore, BLK, the typical product of hydromagmatic fragmentation and rapid quenching associated with the dynamic heat transfer model (Fitch and Fagents, 2020), are characterized here by a microlite-rich groundmass instead of the typical glass-bearing groundmass and possibly derive from fine fragmentation of poorly vesicular portions of the lava. As discussed, the products of the explosions do not show any evidence of an important role of MFCI processes (intended as repeated cycles of intimate fuel-coolant mixing, vapor film generation, and collapse driving to a thermohydraulic explosion; Wohletz, 1986; Zimanowski et al., 2015). This prompts us to interpret the main mechanism of the explosion as being related to a static heat transfer, which promotes vapor generation and pressure build-up. The presence of a small, several-meters-high relief on the opposite side of the explosion vent sites suggests that the locus of snow melting, water vaporization, and vapor collection below the moving lava flow was controlled by the pre-existing topography (Fig. S5) and allowed the collection of water and vapor from melting ice in the more depressed portions at the contact with the substratum. On the other hand, the presence of an upper permeability barrier formed

by active, fluid, poorly crystallized lava close to the contact with the snow/ice is suggested by the concentration of crystal-poor, glass-bearing lava clasts (FLU and GLY) in the most fragmented material, which possibly derived from the fine fragmentation and rapid quenching of those portions of the lava in close proximity to the site of vapor expansion. Edwards et al. (2014) suggested that the interaction of pahoehoe lava with a snow-ice substratum is generally more efficient for producing snow melt and melt-water vaporization with respect to aa lava flows. We propose here that the presence of predisposing morphological features in the substratum of the lava flow, like pre-existing depressions, associated with a sustained lava supply able to guarantee a highly efficient heat transfer, play a primary role in the efficient collection of meltwater and the explosive vaporization that also occurs in the case of aa lava flows. Sudden collapse of the lower, partially solidified portions of the advancing lava flow into the water-saturated, underlying snowpack (as proposed by Edwards et al., 2015) could strongly enhance heat transfer, leading to a more rapid vaporization. Although in the present case there is no indication of the occurrence of effective MFCI processes, as discussed above, we suggest that the presence of specific morphological conditions of the substrate below lava flows advancing on snow/ice-covered terrains may also represent a necessary condition for the occurrence of this type of explosive activity.

7.2. Internal Structure of the Lava Flow

The products of the explosions described provide a unique opportunity to study samples of an active lava flow during its emplacement, and thus offer insight into its internal vertical structure. Based on petrographic and textural features, the comparison of coarse and fine material shows that the ejected clasts are dominated by largely crystallized, scoria-like magma (PV and SV fragments for the coarse material and VES, BLK, and ALT particles for the fine material). Plagioclase microlites from the groundmass have slightly different CSD curves for the different types of clasts, while the CSD of clinopyroxene is very similar from clast to clast. This can be interpreted in terms of different processes driving plagioclase crystallization, in contrast to a common process controlling clinopyroxene nucleation and growth. The very similar crystallization parameters of mafic phases in the different clast types suggest they crystallized during the syn-eruptive, degassing-dominated phases of magma ascent (higher N_v and small crystal size). Conversely, plagioclase can be interpreted as the dominant microlite phase during emplacement and cooling of the lava flow, with quite average

size values for GLY and FLU clasts (43.2 μm and 94.9 μm , respectively; Table 1) and intermediate values (between 67 μm and 80 μm ; Table 1) for all of the other clast types. If this is the case, the observed differences between the clast types could reflect zones of different thermal gradients inside the lava flow. Although the VES, BLK, and ALT fragments differ in their external morphology and vesicularity, their very similar groundmass textural features (microlite number density, microlite size distribution, and microlite shape, etc.) are indicative of crystallization dominated by high-nucleation and low-growth rates of microlites, which possibly developed under high-undercooling conditions. Conversely, the textural features of FLU clasts (large plagioclase microlites) can be reconciled with crystallization under the low-undercooling conditions typical of the internal portions of the lava flow. GLY clasts, characterized by the smaller plagioclase microlites, instead record conditions of rapid quenching of the magma, possibly at the base of the flow.

The different textures well summarize the internal variability associated with the different portions of aa lavas (Lipman and Banks, 1987). They are characterized by a significant temperature gradient that is reflected in different degrees of undercooling and hence crystallization dynamics (Fig. 15). So, the poorly vesicular, poorly crystallized, glass-bearing fragments (G, GLY, and FLU), which in total sum up to 14 wt% of the ejected products, represent the internal, hotter portions of the active lava flow. They correspond to the portions of the lava closer to the base of the lava flow (and hence to the explosion site), as they are highly fragmented by the vapor expansion, which results in glass-bearing fragments deformed by fluid. The scoriaceous, variably altered fragments (SV, ALT, and part of the BLK) are conversely representative of the coarsely brecciated, degassed lava portions closer to the external surface of the active lava

flow. Groundmass textures related to processes of thermal recycling (D’Orlando et al., 2014) are evident on some of these clasts, which typically undergo several cycles of cooling and heating during lava movement. To sum up componentry data for coarser and finer grained clasts, these particles reach ~ 40 wt% of the total erupted mass. Finally, the remainder of the scoriaceous material (PV, VES, and part of BLK), representing ~ 46 wt% of the total erupted mass, could derive from the shattering of the massive, colder, and partially crystallized intermediate portion of the lava flow (Fig. 15). These percentages match the lateral position of the explosion vent sites, close to a levee. Here, the internal, hotter, active portion of the flow was possibly reduced in thickness (Fig. 15). Instead, the large quantity of coarse (lapilli and block) fragments of the SV type possibly reflects a lower efficiency of fragmentation for the upper portion of the lava flow, due to a greater distance from the explosion site, at the base of the flow.

7.3. Dynamics of the Explosion and Hazard Implications

The characteristics of the products erupted during the 16 March 2017 explosion and the observed dynamics of the event suggest that the different explosions (at least three) were driven by the sudden expansion of vapor pockets that accumulated below the lava flow, close to its western levee. As each explosion occurred from distinct sites at distances of a few tens of meters from each other, we exclude the possible occurrence of MFCEI explosions driven by the pouring of liquid magma into the cavity left by a preceding explosion. This mechanism is commonly proposed for the formation of rootless cones (Fagents and Thordarson, 2007). Vinogradov et al. (1990) described explosions resulting in the interaction of lava and ice as a three-stage

process: (1) melting of ice and heating of meltwater to boiling temperature, (2) evaporation of water and consequent volume increase, and (3) breaching of the lava and ejection of a debris-vapor mixture. The gentle east–west topographic gradient transversal to the lava flow, and the presence of a small depression channeling the lava flow (Fig. S5), possibly favored the rapid collection and accumulation of meltwater below the lateral portion of the lava flow and its subsequent vaporization, which confirms the importance of favorable morphological conditions for the occurrence of this type of explosion. For conditions similar to those observed at Etna, the timing of the completion of the second stage was calculated by Vinogradov et al. (1990) to be about one hour, which is in general agreement with the timing of the inundation of the area by the lava flow before the explosions. Times on the order of a few hours were also estimated for the melting (and following vaporization) of several centimeters of the ice/snow cover by the flowing lava. Values of the same order of magnitude (hours) can also be estimated using the average ice melting rates (in the range of 10^{-4} ms^{-1} to 10^{-5} ms^{-1}) calculated by Höskuldsson and Sparks (1997) for subglacial basaltic flows.

The dispersal of ballistic blocks around the explosion site can be used to infer additional information about the dynamics of the explosions. The continuous transition in the energy transfer efficiency from the expanding gas to the sampled blocks (Fig. 14) indicates that the different populations of blocks recognized in the field possibly derive from different portions of the lava flow generated by a single explosion (probably the most energetic one of the sequence studied) rather than representing the cumulative products of different explosions involving various volumes of external water/vapor. We suggest that the largest proximal blocks came from peripheral parts of the main explosion site, for which the fragmentation potential as well as the accelerating pressure were reduced. Conversely, the more distal blocks of samples PH13, PH15, PH16, and PH19 (sampled at distances of between ~ 70 m and ~ 145 m) possibly derived from the deeper portion of the lava flow closer to the explosion site, probably along with ash and lapilli. The absence of significant depressions due to snow melting at the impact site of the coarsest ejecta also indirectly suggests the provenance of these clasts from the upper, brecciated surface of the lava flow, where the clasts were already partially cooled when they became involved in the explosion. Conversely, the finer grained material (lapilli to ash) was more regularly dispersed and was possibly concentrated in the central portion of the explosion plume. This material, also enriched in fragments from the inner portion of

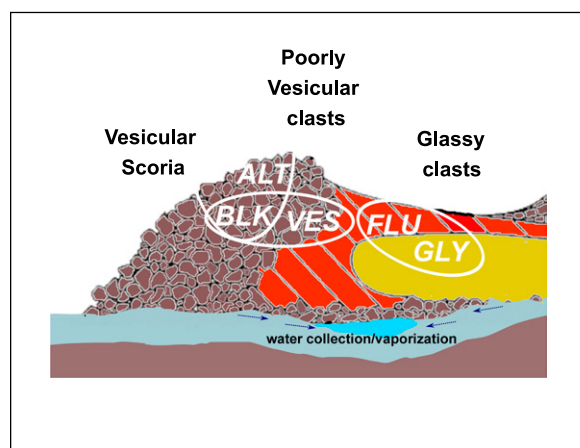


Figure 15. Proposed model for the origin of the explosions and the different types of components recognized in the 16 March 2017 deposits (Redrawn from Lipman and Banks, 1987). Yellow—internal, hotter, non-vesicular active portion of the lava flow; red—massive, crystallized portion of the early crust; brown—outer, brecciated, scoriaceous crust formed by aa rubble. ALT—altered clasts; GLY—glassy clasts; FLU—fluidal clasts; BLK—blocky clasts; VES—vesicular clasts.

the lava flow (i.e., GLY particles; Fig. 15), had a stronger mechanical and thermal coupling with the expanding vapor, so it followed the plume dispersal more closely. Fragmentation mechanisms for vapor expansion from below the lava flow, without the intervention of fragmentation by MFCI processes, could also explain the low abundance of ash in the ejected material.

Important information for risk assessment in the event of future explosions can be directly derived from the data presented. Although the estimated ejection velocity of the clasts was low in comparison to other volcano-related explosions, the impact energy of the measured blocks, up to a distance of >100 m from the lava flow margin, was generally higher than the threshold estimated for provoking injuries to people (impact energy density >0.1 Jmm⁻²; Rezende-Neto et al., 2009) or even skull fractures (impact energy >28 J; Osman et al., 2019). In addition, the measured block areal density, on the order of 1 m⁻² at a distance of a few tens of meters from the lava flow (Fig. 6), suggests that in case of a sudden explosion where tourist groups are present, the probability of serious injury could be very high. In this case, risk could be mitigated by allowing only brief stopovers several tens of meters from the lava flow, and by avoiding the formation of clustered groups.

8. CONCLUSIONS

The 16 March 2017, lava-snow explosion at Etna represents a typical example of a low-intensity, relatively frequent, poorly studied volcanic phenomenon that can produce locally severe impacts, especially in the presence of people. Our study possibly represents a unique case in which complete characterization of the products and deposits has been performed. A few conclusions can be drawn in terms of the mechanisms, dynamics, and possible hazards associated with this type of event:

(1) The lava-snow/ice explosions are related to static heat transfer from the lava to the snow-covered substratum, which occurred under favorable conditions of pre-existing substratum topography. Critical conditions can be reached in just a few hours after the invasion of the area by the lava flow. We suggest that favorable substrate conditions also may be needed in case of more intense explosive activity driven by MFCI processes. In this case, the collection of a significant volume of meltwater at the base of the flow could represent a prerequisite for triggering an intermix of magma and water, magma pre-fragmentation, and successive vapor explosion.

(2) In the presence of favorable substratum conditions, aa lavas can also produce small, although possibly hazardous, explosions.

(3) No clear evidence of MFCI processes is observed in the products, which suggests that dynamic processes of magma-water interaction are possibly only associated with the more complex, prolonged activity typical of rootless cone formation, in which external water availability is longer lasting with respect to the lava-snow interaction of small-scale lava flows.

(4) Dispersal of the coarsest products, with an associated kinetic energy capable of severely harming people, is possible in a range of up to ~100 m from the explosion sites, which suggests that trained personnel accompanying tourists should take adequate safety measures. A safety distance should clearly be estimated and set case by case, considering the morphological, physical, and dynamical features of lava flowing on a glaciated substratum.

Although still an underrated phenomenon, sudden explosions associated with lava flowing over ice/snow-covered terrains occur quite frequently, and the associated risks are strongly related to the increasing opportunities for tourists to flock to this highly spectacular type of volcanic activity. The case studied here clearly highlights some general conditions that enhance the probability of occurrence of such explosions and suggests that the availability of high-resolution topography of the lava flow substratum and accurate knowledge of the average thickness of the snow/ice cover, combined with the results of real-time lava flow path modeling, could help to estimate the probability of such explosions.

ACKNOWLEDGMENTS

The work was partially supported by research funds from the Università di Firenze to R. Cioni and funds provided by the Italian Presidenza del Consiglio dei Ministri—Dipartimento della Protezione Civile (DPC) to all of the authors. The manuscript benefited considerably from the valued comments of Ben Edwards and Armann Höskuldsson and the suggestions of the associate editor. We are also indebted to Lucia Messina for her support in the INGV-OE laboratories and to S. Conway for revising the English language of the text. The authors are very grateful to E. Magri, who provided permission to use, for scientific purposes, some images extracted from a video of the 16 March 2017 explosion. This paper does not necessarily represent DPC official opinion and policies.

REFERENCES CITED

- Andronico, D., Scollo, S., Castro, M.D.L., Cristaldi, A., Lodato, L., and Taddeucci, J., 2014a, Eruption dynamics and tephra dispersal from the 24 November 2006 paroxysm at South-East crater, Mt Etna, Italy: *Journal of Volcanology and Geothermal Research*, v. 274, p. 78–91, <https://doi.org/10.1016/j.jvolgeores.2014.01.009>.
- Andronico, D., Scollo, S., Cristaldi, A., and Lo Castro, M.D., 2014b, Representivity of incompletely sampled fall deposits in estimating eruption source parameters: A test using the 12–13 January 2011 lava fountain deposit from Mt. Etna volcano, Italy: *Bulletin of Volcanology*, v. 76, no. 10, p. 1–14, <https://doi.org/10.1007/s00445-014-0861-3>.
- Andronico, D., Corsaro, R.A., Cristaldi, A., Lo Castro, M.D., Messina, L., Scollo, S., and Spata, G., 2017, L'attività

- esplosiva del Cratere di SE tra il 15 e il 18 marzo 2017: Dispersione del deposito distale di caduta e caratteristiche tessiturali delle ceneri eruttate: Rapporto interno N. 005/2017, http://www2.ct.ingv.it/it/rapporti/vulcanologia/doc_view/9739-1-attivita-esplosiva-del-cratere-di-se-tra-il-15-e-il-18-marzo-2017.html (accessed October 2022).
- Andronico, D., Di Roberto, A., De Beni, E., Behncke, B., Bertagnini, A., Del Carlo, P., and Pompilio, M., 2018, Pyroclastic density currents at Etna volcano, Italy: The 11 February 2014 case study: *Journal of Volcanology and Geothermal Research*, v. 357, p. 92–105, <https://doi.org/10.1016/j.jvolgeores.2018.04.012>.
- Andronico, D., Cannata, A., Di Grazia, G., and Ferrari, F., 2021, The 1986–2021 paroxysmal episodes at the summit craters of Mt. Etna: Insights into volcano dynamics and hazard: *Earth-Science Reviews*, v. 220, <https://doi.org/10.1016/j.earscirev.2021.103686>.
- Barberi, F., Bertagnini, A., Landi, P., and Principe, C., 1992, A review on phreatic eruptions and their precursors: *Journal of Volcanology and Geothermal Research*, v. 52, no. 4, p. 231–246, [https://doi.org/10.1016/0377-0273\(92\)90046-G](https://doi.org/10.1016/0377-0273(92)90046-G).
- Belousov, A., Behncke, B., and Belousova, M., 2011, Generation of pyroclastic flows by explosive interaction of lava flows with ice/water-saturated substrate: *Journal of Volcanology and Geothermal Research*, v. 202, no. 1–2, p. 60–72, <https://doi.org/10.1016/j.jvolgeores.2011.01.004>.
- Bisson, M., Spinetti, C., Neri, M., and Bonforte, A., 2016, Mt. Etna volcano high-resolution topography: Airborne LiDAR modelling validated by GPS data: *International Journal of Digital Earth*, v. 9, no. 7, p. 710–732, <https://doi.org/10.1080/17538947.2015.1119208>.
- Blundy, J., Cashman, K., and Humphreys, M., 2006, Magma heating by decompression-driven crystallization beneath andesite volcanoes: *Nature*, v. 443, no. 7107, p. 76–80, <https://doi.org/10.1038/nature05100>.
- Bonadonna, C., Cioni, R., Pistolesi, M., Connor, C., Scollo, S., Pioli, L., and Rosi, M., 2013, Determination of the largest clast sizes of tephra deposits for the characterization of explosive eruptions: A study of the IAVCEI commission on tephra hazard modelling: *Bulletin of Volcanology*, v. 75, 680, <https://doi.org/10.1007/s00445-012-0680-3>.
- Browne, P.R.L., and Lawless, J.V., 2001, Characteristics of hydrothermal eruptions, with examples from New Zealand and elsewhere: *Earth-Science Reviews*, v. 52, no. 4, p. 299–331, [https://doi.org/10.1016/S0012-8252\(00\)00030-1](https://doi.org/10.1016/S0012-8252(00)00030-1).
- Büttner, R., Dellino, P., and Zimanowski, B., 1999, Identifying magma–water interaction from the surface features of ash particles: *Nature*, v. 401, p. 688–690, <https://doi.org/10.1038/44364>.
- CataniaToday, 2017, Etna, esplosione freatica sul fronte lavico: Ferite 10 persone: <http://www.cataniatoday.it/cronaca/etna-esplosione-ferite-16-marzo-2017.html> (accessed October 2022).
- Caudron, C., Taisne, B., Neuberg, J., Jolly, A.D., Christenson, B., Lecocq, T., Syahbana, D., and Suantika, G., 2018, Anatomy of phreatic eruptions: Earth, Planets, and Space, v. 70, no. 1, p. 1–14, <https://doi.org/10.1186/s40623-018-0938-x>.
- Cioni, R., Sbrana, A., and Vecchi, R., 1992, Morphologic features of juvenile pyroclasts from magmatic and phreatomagmatic deposits of Vesuvius: *Journal of Volcanology and Geothermal Research*, v. 51, no. 1–2, p. 61–78, [https://doi.org/10.1016/0377-0273\(92\)90060-Q](https://doi.org/10.1016/0377-0273(92)90060-Q).
- Conway, C.E., Townsend, D.B., Leonard, G.S., Wilson, C.J.N., Calvert, A.T., and Gamble, J.A., 2015, Lava-ice interaction on a large composite volcano: A case study from Ruapehu, New Zealand: *Bulletin of Volcanology*, v. 77, no. 3, p. 1–18, <https://doi.org/10.1007/s00445-015-0906-2>.
- Corsaro, R.A., Andronico, D., Behncke, B., Branca, S., Caltabiano, T., Ciancitto, F., Cristaldi, A., De Beni, E., La Spina, A., Lodato, L., Miraglia, L., Neri, M., Salerno, G., Scollo, S., and Spata, G., 2017, Monitoring the December 2015 summit eruptions of Mt. Etna (Italy): Implications for eruptive dynamics: *Journal of Volcanology and Geothermal Research*, v. 341, p. 53–69, <https://doi.org/10.1016/j.jvolgeores.2017.04.018>.
- Couch, S., Sparks, R.S.J., and Carroll, M.R., 2001, Mineral disequilibrium in lavas explained by convective

- self-mixing in open magma chambers: *Nature*, v. 411, p. 1037–1039, <https://doi.org/10.1038/35082540>.
- De Beni, E., Cantarero, M., Neri, M., and Messina, A., 2021, Lava flows of Mt Etna, Italy: The 2019 eruption within the context of the last two decades (1999–2019): *Journal of Maps*, v. 17, no. 3, p. 65–76, <https://doi.org/10.1080/17445647.2020.1854131>.
- D’Orlando, C., Bertagnini, A., Cioni, R., and Pompilio, M., 2014, Identifying recycled ash in basaltic eruptions: *Scientific Reports*, v. 4, no. 1, p. 1–8, <https://doi.org/10.1038/srep05851>.
- Dundas, C.M., and Keszthelyi, L.P., 2013, Modeling steam pressure under martian lava flows: *Icarus*, v. 226, no. 1, p. 1058–1067, <https://doi.org/10.1016/j.icarus.2013.06.036>.
- Edwards, B., Magnússon, E., Thordarson, T., Gudmundsson, M.T., Höskuldsson, A., Oddsson, B., and Haklar, J., 2012, Interactions between lava and snow/ice during the 2010 Fimmvörðuháls eruption, south-central Iceland: *Journal of Geophysical Research: Solid Earth*, v. 117, no. B4, <https://doi.org/10.1029/2011JB008985>.
- Edwards, B., Karson, J., Wysocki, R., Lev, E., Bindeman, I., and Kueppers, U., 2013, Insights on lava–ice/snow interactions from large-scale basaltic melt experiments: *Geology*, v. 41, no. 8, p. 851–854, <https://doi.org/10.1130/G34305.1>.
- Edwards, B., Belousov, A., Belousova, M., and Melnikov, D., 2015, Observations on lava, snowpack and their interactions during the 2012–13 Tolbachik eruption, Klyuchevskoy Group, Kamchatka, Russia: *Journal of Volcanology and Geothermal Research*, v. 307, p. 107–119, <https://doi.org/10.1016/j.jvolgeores.2015.08.010>.
- Edwards, B.R., Belousov, A., and Belousova, M., 2014, Propagation style controls lava–snow interactions: *Nature Communications*, v. 5, no. 1, p. 1–5, <https://doi.org/10.1038/ncomms6666>.
- Fagents, S.A., and Thordarson, T., 2007, Rootless volcanic cones in Iceland and on Mars, in Chapman, M., ed., *The Geology of Mars: Evidence from Earth-Based Analogs*: Cambridge, UK, Cambridge University Press, p. 151–177, <https://doi.org/10.1017/CBO9780511536014.007>.
- Fagents, S.A., Lanagan, P., and Greeley, R., 2002, Rootless cones on Mars: A consequence of lava-ground ice interaction, in Smellie, G.L., and Chapman, M.G., eds., *Volcano-Ice Interaction on Earth and Mars*: Geological Society, London, Special Publication 202, p. 295–317, <https://doi.org/10.1144/GSL.SP.2002.202.01.15>.
- Fierstein, J., and Nathenson, M., 1992, Another look at the calculation of fallout tephra volumes: *Bulletin of Volcanology*, v. 54, p. 156–167, <https://doi.org/10.1007/BF00278005>.
- Fitch, E.P., and Fagents, S.A., 2020, Using the characteristics of rootless cone deposits to estimate the energetics of explosive lava–water interactions: *Bulletin of Volcanology*, v. 82, no. 12, p. 1–12, <https://doi.org/10.1007/s00445-020-01422-3>.
- Fitch, E.P., Fagents, S.A., Thordarson, T., and Hamilton, C.W., 2017, Fragmentation mechanisms associated with explosive lava–water interactions in a lacustrine environment: *Bulletin of Volcanology*, v. 79, no. 1, p. 1–16, <https://doi.org/10.1007/s00445-016-1087-3>.
- Greeley, R., and Fagents, S.A., 2001, Icelandic pseudocraters as analogs to some volcanic cones on Mars: *Journal of Geophysical Research: Planets*, v. 106, no. E9, p. 20,527–20,546, <https://doi.org/10.1029/2000JE001378>.
- Hamilton, C.W., Thordarson, T., and Fagents, S.A., 2010, Explosive lava–water interactions I: Architecture and emplacement chronology of volcanic rootless cone groups in the 1783–1784 Laki lava flow, Iceland: *Bulletin of Volcanology*, v. 72, no. 4, p. 449–467, <https://doi.org/10.1007/s00445-009-0330-6>.
- Hantusch, M., et al., 2021, Low-energy fragmentation dynamics at Copahue Volcano (Argentina) as revealed by an infrasonic array and ash characteristics: *Frontiers of Earth Science*, v. 9, p. 92.
- Heiken, G., Wohletz, K., and Eichelberger, J., 1988, Fracture fillings and intrusive pyroclasts, Inyo Domes, California: *Journal of Geophysical Research: Solid Earth*, v. 93, no. B5, p. 4335–4350, <https://doi.org/10.1029/JB093iB05p04335>.
- Higgins, M.D., 2000, Measurement of crystal size distributions: *The American Mineralogist*, v. 85, no. 9, p. 1105–1116, <https://doi.org/10.2138/am-2000-8-901>.
- Höskuldsson, A., and Sparks, R.S.J., 1997, Thermodynamics and fluid dynamics of effusive subglacial eruptions: *Bulletin of Volcanology*, v. 59, p. 219–230, <https://doi.org/10.1007/s004450050187>.
- Höskuldsson, A., Sparks, R.S., and Carroll, M.R., 2006, Constraints on the dynamics of subglacial basalt eruptions from geological and geochemical observations at Kverkfjöll, NE-Iceland: *Bulletin of Volcanology*, v. 68, p. 689–701, <https://doi.org/10.1007/s00445-005-0043-4>.
- INGV-OE, 2020, Bollettino settimanale sul monitoraggio vulcanico, geochimico e sismico del vulcano Etna. 23/11/2020–29/11/2020: Istituto Nazionale di Geofisica e Vulcanologia, Rep. 49/2020, <https://www.ct.ingv.it/index.php/monitoraggio-e-sorveglianza/prodotti-del-monitoraggio/bollettini-settimanali-multidisciplinari/394-bollettino-settimanale-sul-monitoraggio-vulcanico-geochimico-e-sismico-del-vulcano-etna20201201file>.
- Kauahikaua, J., 2007, Lava Flow Hazard Assessment, as of August 2007, for Kīlauea East Rift Zone Eruptions, Hawai‘i Island: U.S. Geological Survey Open-File Report 1264, no. 9, <https://doi.org/10.3133/ofr20071264>.
- La Repubblica, 2017, Etna: Esplosione di lava a 2700 metri, dieci feriti. Il video dello scoppio. Continua l’eruzione: https://palermo.repubblica.it/cronaca/2017/03/16/news/etna_avanzano_due_bracci_lavici_boati_e_tremore_ad_alta_quota-160683836/ (accessed October 2022).
- Leibrandt, S., and Le Pennec, J.L., 2015, Towards fast and routine analyses of volcanic ash morphometry for eruption surveillance applications: *Journal of Volcanology and Geothermal Research*, v. 297, p. 11–27, <https://doi.org/10.1016/j.jvolgeores.2015.03.014>.
- Lipman, P.W., and Banks, N.G., 1987, AA Flow Dynamics, Mauna Loa 1984: U.S. Geological Survey Professional Paper 1350, p. 1527–1567.
- Liu, E.J., Cashman, K.V., and Rust, A.C., 2015, Optimising shape analysis to quantify volcanic ash morphology: *GeoResJ*, v. 8, p. 14–30, <https://doi.org/10.1016/j.grj.2015.09.001>.
- Lo Castro, M.D., and Andronico, D., 2008, Operazioni di base per la misura della distribuzione granulometrica di particelle vulcaniche tramite il CAMSIZER: Rapporti Tecnici INGV 79, p. 1–35.
- Lorenz, V., 1987, Pheatomagmatism and its relevance: *Chemical Geology*, v. 62, no. 1–2, p. 149–156, [https://doi.org/10.1016/0009-2541\(87\)90066-0](https://doi.org/10.1016/0009-2541(87)90066-0).
- Lyman, A.W., Kerr, R.C., and Griffiths, R.W., 2005, Effects of internal rheology and surface cooling on the emplacement of lava flows: *Journal of Geophysical Research: Solid Earth*, v. 110, no. B8, <https://doi.org/10.1029/2005JB003643>.
- Marsh, B.D., 1988, Crystal size distribution (CSD) in rocks and the kinetics and dynamics of crystallization: Contributions to Mineralogy and Petrology, v. 99, no. 3, p. 277–291, <https://doi.org/10.1007/BF00375362>.
- Mastin, L.G., 2001, EJECT! A Simple Calculator of Ballistic Trajectories for Blocks Ejected during Volcanic Eruptions: U.S. Geological Survey Open-File Report 2001-45, 16 p., <https://doi.org/10.3133/ofr0145>.
- Mattox, T.N., and Mangan, M.T., 1997, Littoral hydrovolcanic explosions: A case study of lava–seawater interaction at Kīlauea Volcano: *Journal of Volcanology and Geothermal Research*, v. 75, no. 1–2, p. 1–17, [https://doi.org/10.1016/S0377-0273\(96\)00048-0](https://doi.org/10.1016/S0377-0273(96)00048-0).
- Morelle, R., Mount Etna: BBC crew caught up in volcano blast, 16 March 2017: BBC, <https://www.bbc.com/news/world-europe-39293086>.
- Morgan, D.J., and Jerram, D.A., 2006, On estimating crystal shape for crystal size distribution analysis: *Journal of Volcanology and Geothermal Research*, v. 154, no. 1–2, p. 1–7, <https://doi.org/10.1016/j.jvolgeores.2005.09.016>.
- Noguchi, R., Höskuldsson, A., and Kurita, K., 2016, Detailed topographical, distributional, and material analyses of rootless cones in Myvatn, Iceland: *Journal of Volcanology and Geothermal Research*, v. 318, p. 89–102, <https://doi.org/10.1016/j.jvolgeores.2016.03.020>.
- Osman, S., Rossi, E., Bonadonna, C., Frischknecht, C., Andronico, D., Cioni, R., and Scollo, S., 2019, Exposure-based risk assessment and emergency management associated with the fallout of large clasts at Mount Etna: *Natural Hazards and Earth System Sciences*, v. 19, no. 3, p. 589–610, <https://doi.org/10.5194/nhess-19-589-2019>.
- Pyle, D.M., 1989, The thickness, volume and grain size of tephra fall deposits: *Bulletin of Volcanology*, v. 51, no. 1, p. 1–15, <https://doi.org/10.1007/BF01086757>.
- Rezende-Neto, J., Silva, F.D., Porto, L.B., Teixeira, L.C., Tien, H., and Rizoli, S.B., 2009, Penetrating injury to the chest by an attenuated energy projectile: A case report and literature review of thoracic injuries caused by “less-lethal” munitions: *World Journal of Emergency Surgery*, v. 4, p. 1–5, <https://doi.org/10.1186/1749-7922-4-26>.
- Schneider, C.A., Rasband, W.S., and Eliceiri, K.W., 2012, NIH Image to ImageJ: 25 years of image analysis: *Nature Methods*, v. 9, no. 7, p. 671–675, <https://doi.org/10.1038/nmeth.2089>.
- Smellie, J.L., and Edwards, B.R., 2016, *Glaciovolcanism on Earth and Mars*: Cambridge, UK, Cambridge University Press, <https://doi.org/10.1017/CBO9781139764384>.
- Stevenson, J.A., Smellie, J.L., McGarvie, D.W., Gilbert, J.S., and Cameron, B.I., 2009, Subglacial intermediate volcanism at Kerlingarfjöll, Iceland: Magma–water interactions beneath thick ice: *Journal of Volcanology and Geothermal Research*, v. 185, no. 4, p. 337–351, <https://doi.org/10.1016/j.jvolgeores.2008.12.016>.
- Tarquini, S., Favalli, M., Mazzarini, F., Isola, I., and Fornaciari, A., 2012, Morphometric analysis of lava flow units: Case study over LIDAR-derived topography at Mount Etna, Italy: *Journal of Volcanology and Geothermal Research*, v. 235–236, p. 11–22, <https://doi.org/10.1016/j.jvolgeores.2012.04.026>.
- Thorarinnsson, S., 1953, The crater groups in Iceland: *Bulletin of Volcanology*, v. 14, p. 3–44, <https://doi.org/10.1007/BF02596003>.
- Vinogradov, V.N., Muravyev, Y.D., Nikitina, I.M., and Salamatin, A.N., 1990, Production of phreatic explosions in the interaction of lava and ice: *Volcanology and Seismology*, v. 9, no. 1, p. 89–98.
- Wilson, L., and Head, J.W., III, 2002, Heat transfer and melting in subglacial basaltic volcanic eruptions: Implications for volcanic deposit morphology and meltwater volumes, in Smellie, G.L., and Chapman, M.G., eds., *Volcano-Ice Interaction on Earth and Mars*: Geological Society, London, Special Publication 202, p. 5–26, <https://doi.org/10.1144/GSL.SP.2002.202.01.02>.
- Wilson, L., and Head, J.W., III, 2007, Heat transfer in volcano–ice interactions on Earth: *Annals of Glaciology*, v. 45, p. 83–86, <https://doi.org/10.3189/172756407782282507>.
- Wilson, L., Smellie, J.L., and Head, J.W., 2013, Volcano-ice interactions, in Fagents, S.A., Gregg, T.K.P., and Lopes, R.M.C., eds., *Modelling Volcanic Processes: The Physics and Mathematics of Volcanism*: Cambridge, UK, Cambridge University Press, p. 275–299, <https://doi.org/10.1017/CBO9781139021562.013>.
- Wohletz, K.H., 1986, Explosive magma–water interactions: Thermodynamics, explosion mechanisms, and field studies: *Bulletin of Volcanology*, v. 48, no. 5, p. 245–264, <https://doi.org/10.1007/BF01081754>.
- Wörner, G., and Viereck, L., 1987, Subglacial to emergent volcanism at Shield Nunatak, Mt Melbourne volcanic field, Antarctica: *Polarforschung*, v. 57, no. 1–2, p. 27–41.
- Zimanowski, B., Büttner, R., Dellino, P., White, J.D., and Wohletz, K.H., 2015, Magma–water interaction and phreatomagmatic fragmentation, in Sigurdsson, H., ed., *The Encyclopedia of Volcanoes* (second edition): London, Academic Press, p. 473–484, <https://doi.org/10.1016/B978-0-12-385938-9.00026-2>.

SCIENCE EDITOR: MIHAI DUCEA
ASSOCIATE EDITOR: MICHAEL ÖRT

MANUSCRIPT RECEIVED 26 APRIL 2023
REVISED MANUSCRIPT RECEIVED 14 AUGUST 2023
MANUSCRIPT ACCEPTED 29 AUGUST 2023